Density Functional Study of the Valence-Tautomeric Interconversion Low-Spin $[Co^{III}(SQ)(Cat)(phen)] \rightleftharpoons$ High-Spin $[Co^{II}(SQ)_2(phen)]$

David M. Adams,[1] Louis Noodleman,*,[2] and David N. Hendrickson*,[1]

Department of Chemistry and Biochemistry−0358, University of California at San Diego, La Jolla, California 92093-0358, and Department of Molecular Biology−TPC15, The Scripps Research Institute, La Jolla, California 92037

Received September 26, 1996[⊗]

The results of self-consistent field (SCF) nonlocal density functional molecular orbital calculations are presented for the various spin states and tautomeric forms of a cobalt complex with two *o*-quinone-derived ligands. In addition, new variable-temperature solution magnetic susceptibility, EPR, and electronic absorption data are presented to characterize the *low-spin* $[Co^{III}$(3,5-DTBSQ)(3,5-DTBCat)(phen)] to *high-spin* $[Co^{II}$(3,5-DTBSQ)$_2$-(phen)] valence-tautomeric interconversion, where 3,5-DTBSQ$^-$ and 3,5-DTBCat^{2-} are the semiquinonate and catecholate forms of 3,5-di-*tert*-butyl-*o*-benzoquinone, respectively, and phen is 1,10-phenanthroline. The solution magnetic susceptibility data were fitted to give $\Delta H = 2238$ cm^{-1} and $\Delta S = 118.1$ J mol^{-1} K^{-1} for the *ls*-$Co^{III} \rightleftharpoons$ *hs*-Co^{II} equilibrium. Appreciable changes are seen in the electronic absorption spectrum as the complex changes between the two tautomeric forms. Unrestricted SCF calculations gave $J = -594$ cm^{-1} for the parameter characterizing the antiferromagnetic exchange interaction between *hs*-Co^{II} ion ($S = {}^3/_2$) and each of the two coordinated semiquinonate ($S = {}^1/_2$) ligands in the *hs*-Co^{II} tautomer. The calculations indicated that the *ls*-Co^{III} tautomer state is the most stable with an energy separation of $\Delta E = 4428$ cm^{-1} (0.55 eV) between this *ls*-Co^{III} state and the $S = {}^1/_2$ component of the *hs*-Co^{II} spin ladder. This ΔE value compares favorably with the ΔH value evaluated from variable-temperature susceptibility data.The calculations indicate that, while there are still localized electronic structural features reflecting the different metal and ligand oxidation states in the *ls*-Co^{III} and *hs*-Co^{II} tautomeric forms, appreciable covalent interactions exist between the cobalt ion and the ligands. Finally, the results of the calculations were used to assign the electronic transitions seen for the *ls*-Co^{III} and *hs*-Co^{II} tautomers.

Introduction

The electronic structure of transition metal complexes with noninnocent, *i.e.*, redox-active, ligands has been of continuing interest. Redox activity is found for quinone,[3] nitrosyl,[4] 1,2-dithiolenes,[5] diimines,[6] porphyrins,[7] and phthalocyanines.[8] *o*-Quinones form an important class of redox-active ligands that can exist in three different oxidation states. Addition of one electron to a π^* molecular orbital of an *o*-quinone (Q) gives the paramagnetic ($S = {}^1/_2$) *o*-semiquinonate (SQ^-) ligand that can be further reduced to the *o*-catecholate (Cat^{2-}) ligand. First-row transition metal complexes of *o*-quinones have localized bonding descriptions where ligands and metal have idealized oxidation states and unpaired spin density resides in localized regions of the molecule.[3] Second- and third-row transition metal complexes of *o*-quinones are characterized by more delocalized bonding.[6] These conclusions are based on an extensive X-ray structural and spectroscopic data base.[3]

Valence tautomerism is the most interesting property exhibited by metal complexes with redox-active ligands. Transition metal complexes of Co,[9−11] Mn,[12] Fe,[13] Rh and Ir,[14] and Cu[15] with ligands derived from substituted *o*-benzoquinones show valence tautomerism. The nature of a valence-tautomeric interconversion can be best illustrated by Figure 1. Relatively small changes in temperature[9] and pressure[16] lead to an interconversion between the two tautomeric forms of complex **1**, *low-spin* $[Co^{III}$(3,5-DTBSQ)(3,5-DTBCat)(phen)]·$(C_6H_5CH_3)$ and *high-spin* $[Co^{II}$(3,5-DTBSQ)$_2$(phen)]·$(C_6H_5CH_3)$, where 3,5-

⊗ Abstract published in *Advance ACS Abstracts,* August 1, 1997.

(1) University of California at San Diego.
(2) The Scripps Research Institute.
(3) (a) Pierpont, C. G.; Buchanan, R. M. *Coord. Chem. Rev.* **1981**, *38*, 45. (b) Pierpont, C. G.; Lange, C. W. *Prog. Inorg. Chem.* **1994**, *41*, 331.
(4) (a) Gudel, H. U. *Chem. Phys. Lett*. **1990**, *175*, 262. (b) Schoonver, N. M.; Baker, E. C.; Eisenberg, R. *J. Am. Chem. Soc.* **1979**, *101*, 1880.
(5) (a) Burns, R. P.; McAuliffe, C. A. *Adv. Inorg. Chem. Radiochem.* **1979**, *22*, 303. (b) Eisenberg, R. *Prog. Inorg. Chem.* **1970**, *12*, 295. (c) McCleverty, J. A. *Prog. Inorg. Chem.* **1968**, *10*, 49.
(6) (a) Masui, H.; Lever, A. B. P.; Auburn, P. R. *Inorg. Chem.* **1991**, *30*, 2402. (b) Lever, A. B. P.; Auburn, P. R.; Dodsworth, E. S.; Haga, M. A.; Liu, W; Melnik, M.; Nevin, W. A. *J. Am. Chem. Soc.* **1988**, *110*, 8076. (c) Kaim, W. *Coord. Chem. Rev.* **1987**, *76*, 187.(d) Konig, K.; Herzog, S. *J. Inorg. Nucl. Chem.* **1970**, *32*, 601.
(7) (a) *Porphyrins and Metalloporphyrins*; Smith, K. M., Ed.; Elsevier Scientific Publishing Co., Amsterdam, **1975**; pp 610−612. (b) Dawson, J. J.; Sono, M. *Chem. Rev.* **1987**, *87*, 1255.
(8) (a) *The Phthalocyanines*; Moser, F. H.; Thomas, A. L., Eds.; CRC Press: Boca Raton, FL, 1983; Vols. I and II. (b) Kasuga, M.; Tsutsui, M. *Coord. Chem. Rev.* **1980**, *32*, 67.
(9) (a) Adams, D. M.; Dei, A.; Rheingold, A. L; Hendrickson, D. N. *Angew. Chem., Int. Ed. Engl.* **1993**, *32*, 880. (b) Adams, D. M.; Dei, A.; Rheingold, A. L; Hendrickson, D. N. *J. Am. Chem. Soc.* **1993**, *115*, 8221.
(10) Abakumov, G. A.; Cherkasov, V. K.; Bubnov, M. P.; Ellert, O. G.; Dobrokhotova, Z. B.; Zarkharov, L. N.; Struchovkov,Y. T. *Dokl. Akad. Nauk* **1993**, *328*, 12.
(11) (a) Buchanan, R. M.; Pierpont, C. G. *J. Am. Chem. Soc.* **1980**, *102*, 4951. (b) Jung, O. S.; Pierpont, C. G. *Inorg. Chem.* **1994**, *33*, 2227.
(12) (a) Lynch, M. W.; Hendrickson, D. N.; Fitzgerald, B. J.; Pierpont, C. G. *J. Am. Chem. Soc.* **1984**, *106*, 2041. (b) Attia, S. A.; Pierpont, C. G. *Inorg. Chem.* **1995**, *34*, 1172.
(13) (a) Lynch, M. W.; Valentine, M.; Hendrickson, D. N. *J. Am. Chem. Soc.* **1982**, *104*, 6982. (b) Attia, S. A.; Bhattacharya, S.; Pierpont, C. G. *Inorg. Chem.* **1995**, *34*, 4427. (c) Attia, A. S.; Jung, O. S.; Pierpont, C. G. *Inorg. Chim. Acta* **1994**, *226*, 91.
(14) Abakumov, G. A.; Razuvaev, G. A.; Nevodchikov, V. I.; Cherkasov, V. K. *J. Organomet. Chem.* **1988**, *341*, 485.
(15) Abakumov, G. A.; Garnov, V. A.; Nevodchikov, V. I.; Cherkasov, V. K. *Dokl. Akad. Nauk SSSR* **1989**, *304*, 107.
(16) Roux, C.; Adams, D. M.; Itie, J.; Polian, A.; Hendrickson, D. N.; Verdaguer, M. *Inorg. Chem.* **1996**, *35*, 2846.

S0020-1669(96)01181-0 CCC: $14.00 © 1997 American Chemical Society

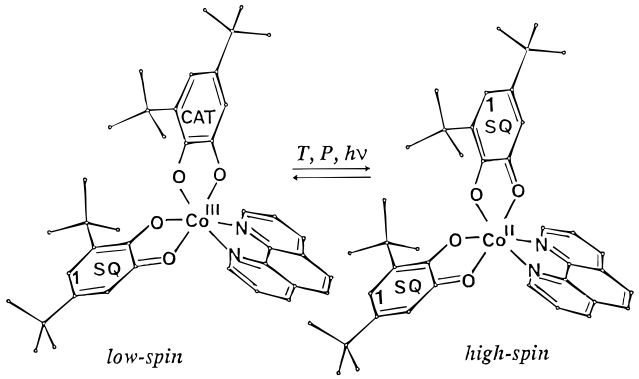

Figure 1. Valence-tautomeric transformation which has been shown to occur in the 1,10-*o*-phenanthroline−bis(3,5-di-*tert*-butyl-*o*-quinone)−cobalt complex under the influence of temperature (*T*), pressure (*P*), and light ($h\nu$).

$DTBSQ^-$ and 3,5-$DTBCat^{2-}$ refer to the semiquinonate and catecholate forms of 3,5-di-*tert*-butyl-*o*-benzoquinone, respectively, and phen is 1,10-phenanthroline. Intramolecular electron transfer converts the *high-spin* Co^{II} into a *low-spin* Co^{III} complex, and one of the ligands is reduced by one electron from a SQ^- to a Cat^{2-} ligand. The interconversion occurs abruptly in a 30 degree temperature range for a microcrystalline sample of the toluene solvate. Furthermore, we have shown[17] that the valence-tautomeric conversion shown in Figure 1 can also be photoinduced in solution and polymeric films with a laser flash. The large changes in the optical, structural, and magnetic properties that accompany the valence-tautomeric interconversion have potential applications in bistable molecular level switching materials.[18,19]

The ground-state potential-energy surface of complex **1** has at least three minima close in energy. The Co^{III} tautomer has Cat^{2-} and SQ^- ligands that, due to the positioning of the *tert*-butyl groups, constitute an asymmetric mixed-valence moiety. The presence of two or more electronic states close in energy leads to significant vibronic interactions and a sensitivity to environment. Other examples of electronic lability are found in mixed-valence[20] and spin-crossover complexes.[21]

The goal of the present paper was to carry out a detailed theoretical study of the electronic structure of the above Co−phen valence tautomers. In fact, there has been no theoretical calculation of the electronic structure of a monomeric spin-crossover or a valence-tautomeric complex. In this paper spin-unrestricted density functional theory[22] is used to calculate the electronic structures of *ls*-[Co^{III}(SQ)(Cat)(phen)], *ls*-[$Co^{II}(SQ)_2$(phen)], *hs*-[$Co^{II}(SQ)_2$(phen)], and the ethylenediamine (en) complex[11b] *ls*-[Co^{III}(SQ)(Cat)(en)]. The calculations presented utilize the Amsterdam density functional (ADF) codes developed in the laboratory of E. J. Baerends.[23] Other transition metal complexes that have been effectively investigated with this program include iron−sulfur complexes,[24] iron and cobalt porphyrins,[25] metal phthalocyanines,[26] $[Ru(bpy)_3]^{2+}$,[27] [X$Mn(CO)_3$(bpy)] (X = Cl, I),[28] $[Mn_4O_3(OAc)_3Cl_7]^{3-}$,[29] and dimeric manganese complexes.[30,31]

Several issues were examined in the present calculations. First, it was important to elucidate the spin-polarized molecular orbital structure of the Co−phen−Sq(Cat) complexes. Do the calculations indicate distinct oxidation states for metal and ligands, and what are the calculated charges and net spin densities? Second, the energy difference between the observed *ls*-[Co^{III}(SQ)(Cat)(phen)] and *hs*-[$Co^{II}(SQ)_2$(phen)] tautomers is calculated and compared to the experimental value. Third, a broken-symmetry formalism is used to calculate the magnitude of the magnetic exchange interactions between $S = {}^1/_2$ ligands and $S = {}^3/_2$ cobalt ion in the *hs*-Co^{II} and $S = {}^1/_2$ cobalt ion in the *ls*-Co^{II} tautomers. Fourth, the effect of the counter ligand (phen *vs* en) on the valence tautomerism is examined. Finally, an interpretation of the electronic absorption spectra is given based on ΔSCF calculations and one-electron orbital energy differences.

Experimental and Computational Details

Synthesis and Characterization. A sample of *hs*-[Co^{II}(3,5-DTBSQ)$_2$(phen)]·($C_6H_5CH_3$) (**1**) was synthesized as previously reported.[9b] The crystal structure has been reported at 173, 238, and 300 K.[9b] The 173 K structure corresponds to the *ls*-[Co^{III}(3,5-DTBSQ)(3,5-DTBCat)(phen)] valence tautomer, while the 300 K structure corresponds to the *hs*-[Co^{II}(3,5-DTBSQ)$_2$(phen)] valence tautomer. The 238 K structure was obtained[9b] at the midpoint of the valence-tautomeric interconversion. It may represent an average of *ls*-Co^{III} and *hs*-Co^{II} forms, or it may represent the *ls*-[Co^{II}(3,5-DTBSQ)$_2$(phen)] intermediate state. The characterization of *ls*-[Co^{III}(3,5-DTBSQ)(3,5-DTBCat)(tmeda)] (**2**), where tmeda is *N*,*N*,*N*′,*N*′-tetramethylethylenediamine, has been reported.[11b] The X-ray structure of this tmeda complex was determined at room temperature.

Magnetic Measurements. Direct current (dc) magnetic susceptibility measurements were carried out on a Quantum Design MPMS SQUID susceptometer equipped with a 55 kG magnet and operating in the range of 1.7−400 K. All measurements were taken at a field of 10 kG. Solutions of complex **1** were prepared in a dry glovebox under an atmosphere of argon by dissolving ∼0.002 g of the complex in ∼0.7 g of toluene-d_8. A specially built sealable quartz tube was used as the sample holder. Deuterated toluene was used to ensure stable reproducible base lines. Background correction data were collected from magnetic susceptibility measurements on the sealed quartz tube containing only toluene-d_8, and these data were subtracted from the magnetic susceptibility data for complex **1**.

Optical Spectroscopy. Electronic absorption spectra in the 300−800 nm range were recorded with a Hewlett-Packard 8452A diode array spectrometer equipped with a Janis model 8DT-SVT-OPT optical

(17) Adams, D. M.; Li, B. L.; Simon, J. D.; Hendrickson, D. N. *Angew. Chem., Int. Ed. Engl.* **1995**, *34*, 1481.
(18) Hendrickson, D. N.; Adams, D. M.; Wu, C. C. in *Magnetism: A Supramolecular Function*; Kahn, O., Ed.; NATO ASI Series; Kluwer Publishing Co.: Dordrecht, The Netherlands, in press.
(19) (a) Hauser, A. *Chem. Phys. Lett.* **1993**, *202*, 173. (b) Hauser, A. *Coord. Chem. Rev.* **1991**, *111*, 275.
(20) (a) Day, P. *Int. Rev. Phys. Chem.* **1981**, *1*, 149. (b) Creutz, C. *Prog. Inorg. Chem.* **1983**, *30*, 1. (c) Richardson, D. E.; Taube, H. *Coord. Chem. Rev.* **1984**, *60*, 107. (d) Hendrickson, D. N. In *Mixed Valence Systems: Applications in Chemistry, Physics, and Biology*; Prassides, K., Ed.; NATO ASI Series; Kluwer Publishing Co.: Dordrecht, The Netherlands, 1991; pp 67−90.
(21) (a) Beattie, J. K. *Adv. Inorg. Chem.* **1988**, *32*, 1−53. (b) Konig, E. *Prog. Inorg. Chem.* **1987**, *35*, 527−622. (c) Rao, C. N. R. *Int. Rev. Phys. Chem.* **1985**, *4*, 19. (d) Gütlich, P. *Struct. Bonding (Berlin)* **1981**, *44*, 83. (e) Bacci, M. *Coord. Chem. Rev.* **1988**, *86*, 245. (f) Maeda, Y.; Takashima, Y. *Comments Inorg. Chem.* **1988**, *7*, 41. (g) Toftlund, H. *Coord. Chem. Rev.* **1989**, *94*, 67−108. (h) Zarembowitch, J. *New J. Chem.* **1992**, *16*, 255−267. (i) Kahn, O. In *Molecular Magnetism*; VCH Publishers: New York, 1993; pp 52−85.
(22) (a) *Density Functional Methods in Chemistry*; Labanowski, J. K., Andzelm, J. W., Eds.; Springer Verlag: New York, 1991. (b) Ziegler, T. *Chem. Rev.* **1991**, *91*, 651.
(23) te Velde, G.; Baerends, E. J. *J. Comput. Phys.* **1992**, *99*, 84.
(24) Noodleman, L.; Peng, C. Y.; Case, D. A.; Mouesca, J. M. *Coord. Chem. Rev.* **1995**, *144*, 199.
(25) Jones, D. H.; Hinman, A. S.; Ziegler, T. *Inorg. Chem.* **1993**, *32*, 2092.
(26) Rosa, A.; Baerends, E. J. *Inorg. Chem.* **1994**, *33*, 584.
(27) Daul, C.; Baerends, E. J.; Vernooijs, P. *Inorg. Chem.* **1994**, *33*, 3538.
(28) Stor, G. J.; Stufkens, D. J.; Vernooijs, P.; Baerends, E. J.; Fraanje, J.; Goubitz, K. *Inorg. Chem.* **1995**, *34*, 1588.
(29) Schmitt, E. A.; Noodleman, L.; Baerends, E. J.; Hendrickson, D. N. *J. Am. Chem. Soc.* **1992**, *114*, 6109.
(30) Zhao, X. G.; Richardson, W. H.; Chen, J. L.; Noodleman, L.; Tsai, H. L.; Hendrickson, D. N. *Inorg. Chem.* **1997**, *36*, 1198.
(31) Rosa, A.; Ricciardi, G.; Baerends, E. J.; Stufkens, D. J. *Inorg. Chem.* **1995**, *34*, 3425.

cryostat. Data were collected on 1×10^{-3} toluene solutions of complex **1**, prepared under an atmosphere of argon. Polymer films of the phenanthroline complex were prepared under an atmosphere of argon by dissolving the complex and polystyrene (1−5 wt %) in methylene chloride and solution casting onto flat glass dishes. The solvent was evaporated, and the plastic films were removed from the glass. Optical absorption experiments in the 200−3000 nm range were performed on a Cary 5e spectrophotometer, equipped with a closed-cycle cryostat.

Nonlocal Density Functional Calculations. The calculations performed in this paper utilized the Amsterdam density functional program package AMOL, developed by te Velde, Baerends, and co-workers.[23] Calculations were performed at two different levels. Calculations were performed using the Xα(α=0.7) local exchange potential. Also, calculations were performed which utilized the more sophisticated local exchange-correlation potential of Vosko−Wilk−Nussair (VWN),[32] and nonlocal exchange and correlation energy terms and corresponding potentials of Becke and Perdew.[33−35] These calculations were of the fully nonlocal self-consistent field type (SCF). In this second case the overall exchange-correlation potential is called VBP. All molecular calculations were spin unrestricted, so as to allow for substantial spin polarization on metal and ligand sites. In spin-polarized density functional theory, the spin-up (α) and spin-down (β) electrons are calculated separately, which is critical for any system with unpaired spin density. For a given potential the calculations are characterized by a density fitting procedure to obtain accurate Coulomb and exchange correlation potentials in each SCF cycle, and the Hamiltonian matrix elements are constructed by numerical integration of the potentials with the basis functions over a grid of points. The kinetic-energy matrix elements are constructed analytically as usual.[36,37]

The bonding energies were calculated with respect to a reference state composed of spin-restricted atoms making up the molecule. Identical grids are used for the molecule and the spin-restricted-atom fragments in the energy difference evaluation.[31,32] These methods are a development of the Ziegler−Rauk transition-state method[38] allowing accurate calculation of the molecular binding energy with respect to the spin-restricted-atom reference state. The reference state subtracts out when energy differences between different states are evaluated.

All calculations were performed either on a Cray YMP supercomputer (formerly at the Scripps Research Institute) or a Cray C-90 supercomputer at the San Diego Supercomputer Center (SDSC). For each of the calculations approximately 1.3 GB of disk storage space was required. Convergence was obtained when the change in the diagonal elements of the density matrix (called ADP) was less than 0.0003. Convergence on the C-90 usually was achieved in ∼100−150 cycles at ∼6 min/cycle. The YMP required approximately twice the time.

Calculations were carried out for the *ls*-[Co^{III}(SQ)(Cat)(phen)] 173 K structure, *hs*-[Co^{II} $(SQ)_2$(phen)] using the atomic coordinates from the 300 K structure, *ls*-[$Co^{II}(SQ)_2$(phen)] with coordinates from the 238 K structure, and *ls*-[Co^{III}(SQ)(Cat)(en)] with atomic coordinates from the 300 K structure[11b] of *ls*-[Co^{III}(3,6-DTBSQ)(3,6-DTBCat)(tmeda)]. In all cases the *tert*-butyl groups were removed from the rings of the 3,6-$DTBSQ^-$ and 3,6-$DTBCat^{2-}$ ligands and replaced with hydrogen atoms at a C−H bond distance of 1.0 Å in order to reduce the size of the calculations. Thus, the *o*-quinone-derived ligands are referred to simply as semiquinonate (SQ^-) and catecholate (Cat^{2-}). In the case of the tetramethylethylenediamine (tmeda) ligand the methyl groups were removed and replaced with hydrogen atoms at a C−H bond distance of 1.1 Å. This ligand is consequently referred to as ethylenediamine (en). The orientation and atomic numbering of the phen complexes and the en complex are shown in Figure 2, parts a and b, respectively. In both cases the catecholate ligand was oriented in the *YZ*-plane and the cobalt ion served as the center of the axis system. Atomic orbitals at each atom were given the same orientation of the axis system. All calculations were carried out with no symmetry restrictions. Crystal structure coordinates were used without alteration. Atomic coordinates were rotated and manipulated with home-written programs in the AWK language and with the help of INSIGHTII (Biosym Inc.). In some cases, in order to aid in the understanding of particular molecular orbitals, calculations were performed with different orientations of the molecule (*i.e.*, semiquinonate in the *YZ*-plane). Identical overall energy and results were obtained, only the contribution of each atomic orbital to a given molecular orbital was altered, yielding a convenient method of determining the nature of the molecular orbital.

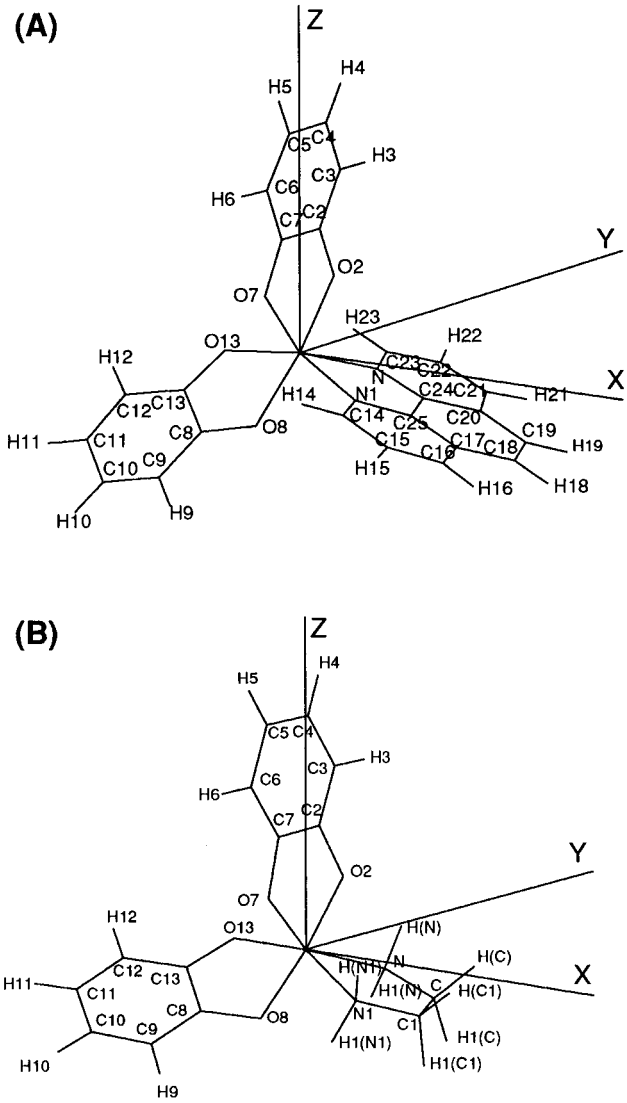

Figure 2. (A) The orientation and labeling of the cobalt−phenanthroline complex used for electronic structure calculations. Atomic positions were taken from the reported[9b] 173, 238, and 300 K X-ray crystal structures. The *tert*-butyl groups were replaced with hydrogen atoms. The catecholate ligand (C2−C7, O2, O7) was oriented within the *ZY*-plane. (B) The ethylenediamine complex orientation and labeling used in the calculations are shown. Atomic positions were taken from crystal structure coordinates of *ls*-[Co(3,6-DTBSQ)(3,6-DTBCat)(tmeda)] where tmeda is tetramethylethylenediamine. The methyl groups of the tmeda and *tert*-butyl groups were replaced with hydrogen atoms.

Slater type basis sets with frozen cores were utilized. For the cobalt atom the basis set consisted of triple-ζ 3d and double-ζ 3s, 3p, 4s functions plus one 4p polarization function. Carbon, oxygen, and nitrogen atoms had double ζ-2s and 2p basis sets, and each hydrogen atom had a double-ζ 1s basis set. The C, N, O, and H basis sets did not contain polarization functions. The actual basis sets used are included in the Supporting Information.

(32) Vosko, S. H.; Wilk, L.; Nusair, M. *Can. J. Phys.* **1980**, *58*, 1200.
(33) Becke, A. D. In *The Challenge of f and d Electrons*; Salahub, D. R., Zerzner, M. C., Eds.; American Chemical Society: Washington, DC, 1989; p 165.
(34) Becke, A. D. *J. Chem. Phys.* **1986**, *84*, 4524.
(35) Perdew, J. P. *Phys. Rev. B* **1986**, *33*, 8822.
(36) Boerrigter, P. M.; te Velde, G.; Baerends, E. J. *Int. J. Quantum Chem.* **1988**, *33*, 87.
(37) te Velde, G. Numerical Integration and Other Methodological Aspects of Band Structure Calculations. Ph.D. Thesis, Vrije University, Amsterdam, 1990.
(38) Ziegler, T.; Rauk, A. *Theor. Chim. Acta* **1977**, *46*, 10.

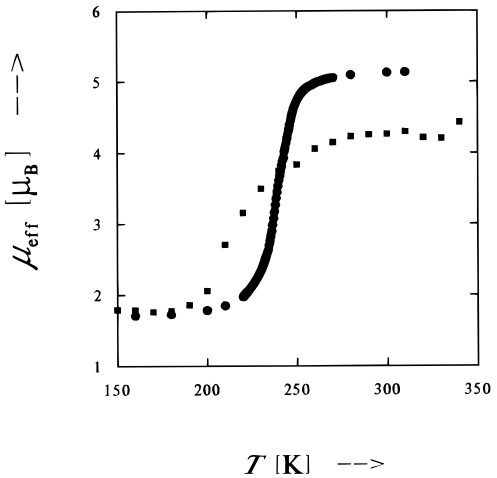

Figure 3. Magnetic susceptibility data for a polycrystalline sample (●) displaying the *ls*-[Co^{III}(3,5-DTBSQ)(3,5-DTCat)(phen)]·($C_6H_5CH_3$) to *hs*-[Co^{II}(3,5-DTBSQ)$_2$(phen)]·($C_6H_5CH_3$) interconversion. Also plotted are the solution magnetic susceptibility data (■) for a 1×10^{-3} M solution of the phenanthroline complex dissolved in toluene-d_8.

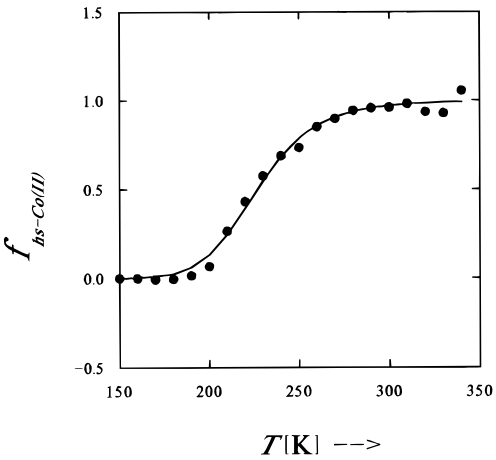

Figure 4. Plot of the fraction of *high-spin* Co^{II} tautomer as a function of temperature for a toluene solution of *hs*-[Co(3,5-DTBSQ)$_2$(phen)] (**1**). The data were fitted (solid line) assuming a two-state equilibrium with the limiting values of the effective magnetic moment as 1.73 μ_B for the *ls*-[Co^{III}(SQ)(Cat)] state and 4.2 μ_B for the *hs*-[Co^{II}(SQ)$_2$] state.

Results and Discussion

Valence Tautomerism in the Solid State, Solution, and Polymer Films. In conjunction with the theoretical results that are presented in this paper, it was important that additional experimental characterization of the valence-tautomeric interconversion of complex **1** be presented. New magnetic susceptibility, EPR, and electronic absorption spectral data are presented.

Since the theoretical calculations were carried out for the molecular complex in a vacuum, it was important to determine the nature of the complex in a relatively non-interacting solvent. Variable-temperature magnetic susceptibility data were collected for a toluene-d_8 solution of complex **1**. These data, together with those reported[9] for a solid sample, are plotted in Figure 3 as the effective magnetic moment per molecule, μ_{eff}, *versus* temperature. It can be seen that both the polycrystalline and solution samples of complex **1** exhibit an μ_{eff} of 1.73 μ_B at the lowest temperatures. This is clearly consistent with a *ls*-[Co^{III}(3,5-DTBSQ)(3,5-DTBCat)(phen)] description, where the Co^{III} ion is low spin and diamagnetic and there is one SQ^- ligand with $S = {}^1/_2$ and $g = 2.0$. In the solid state the complex converts abruptly and completely to the *hs*-Co^{II} form.

The sigmoidal shape of the μ_{eff} *vs* temperature curve for complex **1** in solution is consistent with the equilibrium shown in Figure 1. In solution the μ_{eff} of complex **1** reaches a limiting value of ~4.4 μ_B in the 300−340 K range. Similar sigmoidal μ_{eff} *vs* temperature curves and high-temperature limiting values of μ_{eff} have been determined for other Co valence-tautomeric complexes,[39] such as *hs*-[Co^{II}(3,5-DTBSQ)$_2$(bpy)].[11a] The solution susceptibility data for complex **1** can be fitted to evaluate the enthalpy change (ΔH) and the entropy change (ΔS) for the *ls*-Co^{III} ⇌ *hs*-Co^{II} equilibrium. If we define the fraction of *hs*-Co^{II} complexes at a given temperature as f_{hs} and the fraction of *ls*-Co^{III} complexes as f_{ls} (*i.e.*, $f_{hs} + f_{ls} = 1$), then the equilibrium constant for the valence-tautomeric equilibrium can be written as in eq 1. The fraction of *hs*-Co^{II} tautomeric complexes can

$$K_{eq} = \frac{f_{hs}}{f_{ls}} = \frac{f_{hs}}{1 - f_{hs}} \qquad (1)$$

be evaluated from the susceptibility (χ) data. The free-energy change is given by eq 2. Using the above equations, together

$$\Delta G = -RT \ln(K_{eq}) \qquad (2)$$

with $\Delta G = \Delta H - T\Delta S$, gives f_{hs} as a function of T, ΔH, and ΔS in eq 3.

$$f_{hs} = 1/[\exp(\Delta H/RT - \Delta S/R) + 1] \qquad (3)$$

In Figure 4 the solution magnetic susceptibility data for complex **1** are plotted to display f_{hs} as a function of temperature. Least-squares fitting of the data for complex **1** to eq 3 gives $\Delta H = 26.77$ kJ/mol (2238 cm^{-1}) and $\Delta S = 118.1$ J mol^{-1} K^{-1}. Similar relatively large values of ΔS have been determined for other Co valence-tautomeric complexes.[39] The electronic entropy gain for the valence-tautomeric equilibrium is given by $\Delta S_{elec} = R \ln(w_{hs}/w_{ls})$, where R is the gas constant and w_{hs} and w_{ls} are the electronic degeneracies of the *hs*-Co^{II} and *ls*-Co^{III} tautomers, respectively. For the valence-tautomeric complexes $\Delta S_{elec} = R \ln(16/4) = 11.5$ J mol^{-1} K^{-1}. The *hs*-Co^{II} tautomer also has a greater vibrational entropy than the *ls*-Co^{III} tautomer. The frequencies for the cobalt−ligand atom vibrations of the *hs*-Co^{II} tautomer are less than those of the corresponding vibrational modes of the *ls*-Co^{III} tautomer. It is clear that, when the temperature is increased, the conversion from the smaller *ls*-Co^{III} to the larger *hs*-Co^{II} form of the complex is entropy driven.

Density functional theoretical calculations evaluate the difference in electronic energy (ΔE) between the *ls*-Co^{III} and *hs*-Co^{II} tautomers. If the difference in vibrational frequencies between the two states is neglected, the difference in electronic energies ΔE is approximately equal to the zero point energy difference and thus $\Delta H(T = 0) \simeq \Delta E$. Therefore, the calculated ΔE can be compared to the experimental ΔH at 0 K. Another experimental check on the theoretical calculations can come from EPR data. EPR spectroscopy can be used to provide information on the location of unpaired spin density in transition metal *o*-quinone complexes. In the case of these Co valence tautomeric complexes the main information available from EPR spectra is the cobalt hyperfine interaction. In the spectrum for a frozen glass a signal centered at $g \simeq 2.0$ and split into eight hyperfine lines due to hyperfine coupling to the ^{59}Co ($I = {}^7/_2$) nucleus is seen. Buchanan and Pierpont[11a] reported a cobalt hyperfine splitting of 10.7 G for *ls*-[Co^{III}(3,5-DTBSQ)(3,5-

(39) Adams, D. M.; Hendrickson, D. N. *J. Am. Chem. Soc.* **1996**, *118*, 11515.

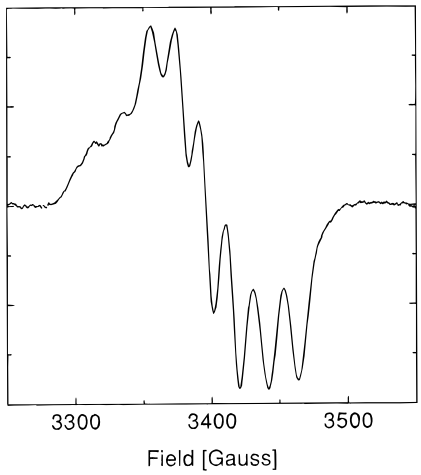

Figure 5. EPR spectrum obtained for a 1×10^{-4} M 2-methylcyclohexane solution of *ls*-[Co^{III}(3,5-DTBSQ)(3,5-DTBCat)(phen)] at 90 K.

DTBCat)(bpy)]. In a later paper Jung and Pierpont[11b] reported that the spectrum of *ls*-[Co^{III}(3,6-DTBSQ)(3,6-DTBCat)(tmeda)] consists of two components, $g_1 = 2.0101$ and $g_2 = 2.005$, each coupled to the cobalt nucleus with constants of $A_1 = 32$ G and $A_2 = 27$ G.

X-band EPR spectra were run for a frozen 2-methylcyclohexane glass of complex **1**. In Figure 5 is shown the 90 K spectrum, where the eight-line cobalt hyperfine splitting is clearly evident. An analysis of this spectrum gives A(Co) = 20 G. The change in the A(Co) value from the tmeda to the phen complex is interesting, for theoretical calculations are presented in this paper for the phen and en (related to tmeda) complexes. It is important to understand how the counter-ligand in these Co complexes affects the valence tautomerism.

Electronic absorption spectra are the third type of data base that is compared to the theoretical electronic results presented in this paper. Previously we showed[9] how the electronic absorption spectrum of a toluene solution of complex **1** changed in the 210−295 K range. At 295 K the spectrum is highly characteristic of the *hs*-Co^{II} tautomer, as indicated by an intense broad band at 780 nm (12 820 cm^{-1}) with a shoulder at ∼660 nm (15 151 cm^{-1}) and a weaker band at 548 nm (18 248 cm^{-1}). On the basis of our calculations (*vide infra*) the band at 780 nm is assigned as a metal-to-ligand charge transfer (MLCT) transition of the *hs*-Co^{II} tautomer. Similarly, the band at 548 nm is associated with the Co^{II} tautomer and is assigned as a ligand field type transition. When the temperature is decreased from 295 to 210 K, the intensity of the 780 nm band decreases appreciably, while a band at ∼600 nm (16 666 cm^{-1}) characteristic of the *ls*-Co^{III} tautomer appears. By 210 K complex **1** has almost completely converted to the *ls*-Co^{III} form.

Large changes in the optical spectrum also occur in the near-infrared (near-IR) region of spectrum. Figure 6 shows the temperature dependence of the electronic absorption spectrum of complex **1** doped into a polystyrene polymer film in the visible and near-IR regions over the temperature range of 295−15 K. The changes in the visible region of the spectrum are similar to those seen for the solution of complex **1**. At 15 K the spectrum largely originates from the *ls*-[Co^{III}(3,5-DTBSQ)-(3,5-DTBCat)(phen)] valence tautomer. The 600 nm (16 666 cm^{-1}) band displays shoulders at ∼560 nm (17 857 cm^{-1}), ∼700 nm (14 285 cm^{-1}), and ∼1000 nm (10 000 cm^{-1}). At low temperatures a band appears at 2500 nm (4000 cm^{-1}) with a shoulder at 1670 nm (5988 cm^{-1}). These near-IR bands are only associated with the *ls*-Co^{III} tautomer. By comparison to the solution spectra, we can give an approximate molar extinction coefficient (ϵ) at the maximum absorption of this low-energy band of ∼2000 cm^{-1} M^{-1}. The exact origin of the intense near-IR band has been a matter of some debate and has tentatively been assigned as either an intervalence charge transfer (IT) band involving excitation from the Cat^{2-} π^* orbital to the SQ^- π^* orbital,[18] or a LMCT transition from the Cat^{2-} π^* orbital to the cobalt e_g^* orbital.[11b] Possible assignments of the electronic absorption bands will be discussed later in this paper.

Theoretical Calculations. (A) Free Ligands. In order to help analyze the results for metal complexes, SCF density functional calculations were carried out also for *o*-benzoquinone. Figure 7 shows the highest lying valence molecular orbitals of the free *o*-quinone ligand which contribute to its oxidation−reduction characteristics and chelating properties with transition metals. Representations are given for all ligand orbitals which contribute significantly to valence molecular orbitals. The symmetry labels are taken from the C_{2v} point group. Shaded regions indicate where the sign of the wave function is negative. Hydrogen atoms have been omitted for clarity. The $9a_1$ orbital is the highest occupied molecular orbital (HOMO) in the neutral *o*-quinone and is localized on the ortho oxygen atoms. The p orbitals of the $9a_1$ orbital lie in the plane of the ring and represent the oxygen lone pairs. This orbital interacts with a metal in a σ fashion. The $3b_1$ orbital is the lowest unoccupied molecular orbital (LUMO) of the neutral *o*-quinone. The p orbitals of the $3b_1$ orbital lie perpendicular to the plane of the ring. The $3b_1$ orbital is a carbon−oxygen π^* antibonding molecular orbital that interacts with a metal atom in a π fashion. The important oxidation−reduction characteristics of *o*-quinones originate from the $3b_1$ orbital. This orbital contains 0, 1, and 2 electrons in the *o*-quinone, *o*-semiquinonate, and *o*-catecholate oxidation levels, respectively. The $2a_2$ orbital is a carbon−oxygen π-bonding orbital that contains a node at the carbon atoms directly attached to the oxygen atoms; it interacts with a metal in a π fashion. The $7b_2$ orbital is localized mainly on the oxygen atoms and is an antisymmetric combination of oxygen p orbitals. Its interaction with a metal is in a σ fashion.

(B) Idealized Spin-Polarized Ligand Field Diagrams. Spin-polarized density functional theory treats spin-up and spin-down electrons separately. This is a necessary requirement for molecules with unpaired spin density where local regions in the system can have a difference in α and β electron densities. The α spin and β spin electrons move in separate self-consistent field (SCF) potentials due to all the electrons and nuclei, and these potentials are locally different. The Pauli exclusion principle requires that electrons of the same spin occupy different spatial orbitals. Electrons of the same spin automatically avoid each other, whereas electrons of opposite spin are not required to occupy different spatial orbitals and consequently are not as effective in avoiding electron−electron repulsion. Consequently α and β spin electrons can occupy different sets of spatial orbitals in order to stabilize the energetics of the system resulting in SCF potentials that have different shapes for α and β electrons. In general, electrons of a particular spin are stabilized in regions where that spin density predominates. For example, α spin electrons are stabilized in regions of α excess spin, and β spin electrons are destabilized in these regions.

Unrestricted SCF density functional calculations were carried out for *ls*-[Co^{III}(SQ)(Cat)(phen)], *ls*-[Co^{III}(SQ)(Cat)(en)], *ls*-[$Co^{II}(SQ)_2$(phen)], and *hs*-[$Co^{II}(SQ)_2$(phen)]. The results of these calculations are presented in the following sections. A few points need to be made before we examine the details. First, the density functional calculations employing the "VBP" potential are first principles calculations with no adjustable

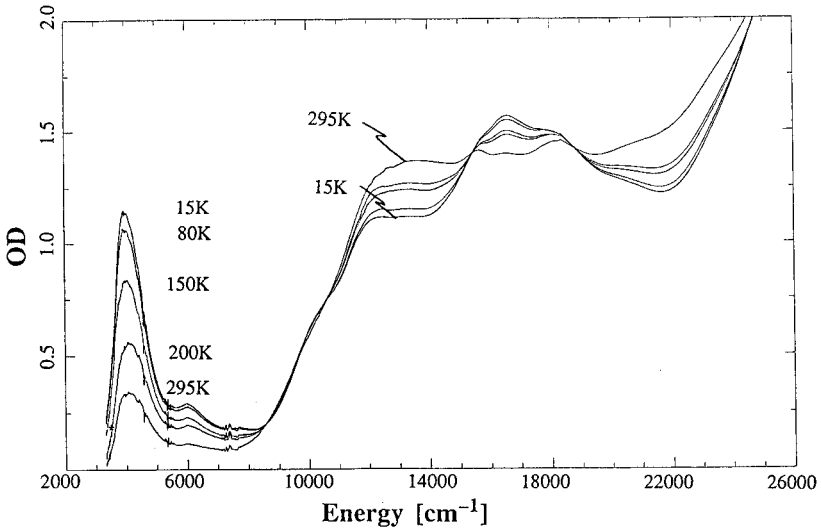

Figure 6. Temperature dependence of the electronic absorption spectrum of [Co(3,5-DTBSQ)$_2$(phen)]·$C_6H_5CH_3$ (**1**) doped into MW 280 000 polystyrene (1.0 wt/wt %) obtained at 295, 200, 150, 80, and 15 K. The optical density is plotted versus energy in cm^{-1}.

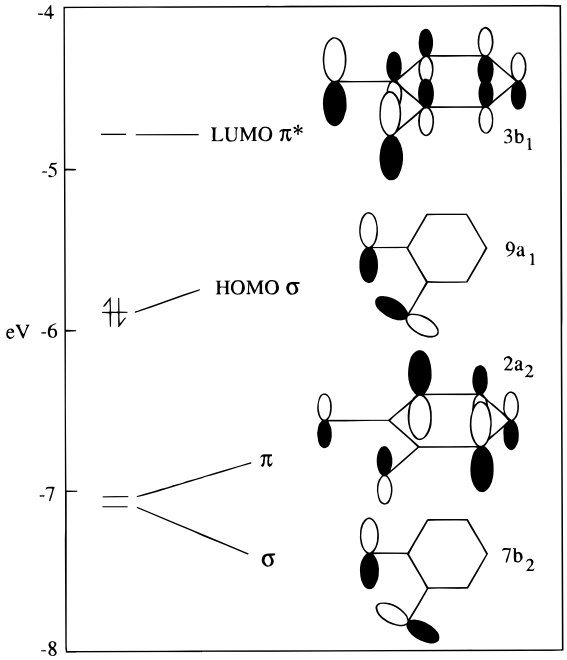

Figure 7. Energy level orderings and molecular orbital descriptions of the frontier molecular orbitals of free *o*-quinone in C_{2v} symmetry. The $3b_1$ π^* orbital accommodates the $1e^-$ and $2e^-$ reductions to form the semiquinonate and catecholate ions, respectively. The $3b_1$ orbital is the magnetic orbital of the semiquinonate.

parameters. The atomic coordinates together with a selection of atomic orbital basis sets are the only input. Second, the atomic coordinates were taken from the single-crystal X-ray structure of the phen complex at 173, 238, and 300 K and in the case of the calculations for the en complex from the 300 K structure of the tmeda complex. Third, in order to calculate the energy difference between *ls*-[Co^{III}(SQ)(Cat)(phen)] and *hs*-[Co^{II}(SQ)$_2$(phen)] it was necessary to calculate the SQ$^-$−Co^{II} magnetic exchange interactions to determine the energies of the $S = {}^1/_2$, ${}^3/_2$, and ${}^5/_2$ components of the spin ladder for *hs*-[Co^{II}-(SQ)(Cat)(phen)]. Fourth, a theoretical calculation was carried out for a hypothetical *ls*-[Co^{II}(SQ)(Cat)(phen)] complex using X-ray coordinates from the 238 K structure[9b] of the phen complex. There is as yet no direct experimental evidence for the existence of such a *ls*-Co^{II} form of the complex.[39]

Since the results from each calculation are extensive and complicated, at the outset it is useful to look at an overview of

Chart 1. Idealized Scheme for the Oxidation States, Spin States, and Electron Configurations of Cobalt d Orbitals and Quinone π^* Orbitals of the Valence Tautomers of a Cobalt Bis-*o*-quinone Complex

	electron configurations		
spin	*ls*-[Co^{III}(SQ)$_A$(Cat)$_B$]	*ls*-[Co^{II}(SQ)$_A$(SQ)$_B$]	*hs*-[Co^{II}(SQ)$_A$(SQ)$_B$]
${}^1/_2$	$d^3\alpha\ d^3\beta$ $\pi^{*2}\alpha\ \pi^{*1}\beta$	$d^3\alpha\ d^4\beta$ $\pi^{*2}\alpha\ \pi^{*0}\beta$	$d^2\alpha\ d^5\beta$ $\pi^{*2}\alpha\ \pi^{*0}\beta$
${}^3/_2$		$d^4\alpha\ d^3\beta$ $\pi^{*2}\alpha\ \pi^{*0}\beta$	$d^2\alpha\ d^5\beta$ $\pi^{*1}\alpha\ \pi^{*1}\beta$
${}^5/_2$			$d^5\alpha\ d^2\beta$ $\pi^{*2}\alpha\ \pi^{*0}\beta$

the frontier orbitals from calculations on the different tautomers. This can be done by examining the idealized energy level diagrams of the spin-polarized ligand field splitting of the cobalt center, including the $3b_1$ π^* energy levels of the two quinones. Understanding the occupation of the cobalt d orbitals and the π^* orbitals of the quinone-derived ligands is essential for understanding the electronic structure of the various valence tautomeric forms. Idealized occupations, spin states, and oxidation levels of some important valence-tautomeric states are presented in Chart 1. Also, Figure 8 graphically illustrates the relative energy level orderings of the metal d orbitals and π^* quinone orbitals of the spin-aligned valence-tautomeric states. The relative energy orderings have been extracted from the calculations. Three situations are illustrated which will be useful in interpreting the calculations discussed later. The vertical axis gives the orbital energies, and the horizontal axis separates levels according to their spin index, α or β. Symmetry labels are taken from idealized O_h symmetry, where the familiar d-orbital splitting into the t_{2g} and e_g set is shown. Figure 8A describes the *ls*-[Co^{III}(Cat)(SQ)] valence-tautomeric state which has the occupation scheme Co^{III} $d^3\alpha\ d^3\beta$ ($S = 0$), Cat $\pi^{*1}\alpha\ \pi^{*1}\beta$ ($S = 0$), SQ $\pi^{*1}\alpha\ \pi^{*0}\beta$ ($S = {}^1/_2$), that is, there are six electrons paired up in the Co t_{2g} orbitals, two electrons of opposite spin in the Cat^{2-} π^* orbital, and one α spin electron in the π^* orbital of the SQ$^-$ ligand. Majority spin was arbitrarily assigned to reside in α. There is only a slight exchange splitting between majority α spin and minority β spin electrons. The majority spin α electrons are stabilized in energy, while the corresponding β minority spin electrons are destabilized. In this case the spin polarization energy is small relative to the ligand field stabilization energy. In contrast, Figure 8C displays the idealized

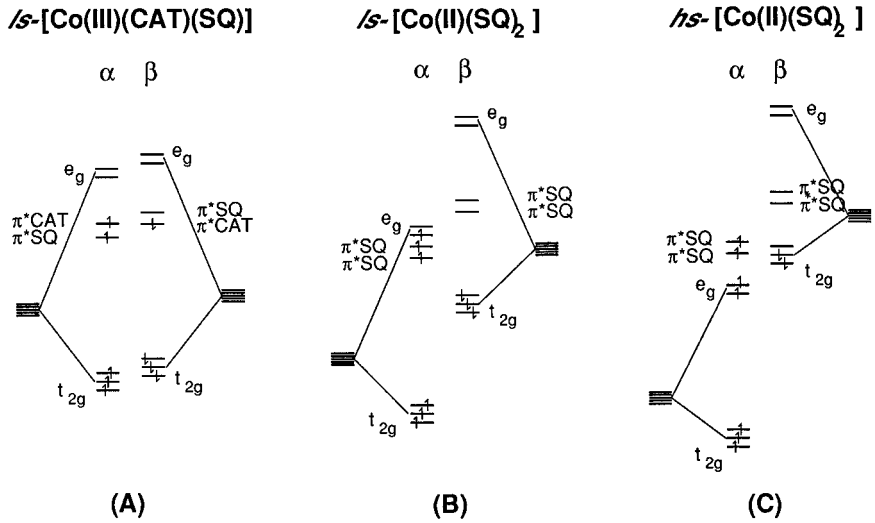

Figure 8. Idealized spin-unrestricted energy level diagrams of some important valence-tautomeric states showing the relative ordering of α spin and β spin energy levels of the ligand field set (O_h symmetry notation) and π^* orbitals of the *o*-quinone ligands: (A) *ls*-[Co^{III}(SQ)(Cat)]; (B) *ls*-[$Co^{II}(SQ)_2$] with a ferromagnetic alignment between spins of the ligands and the cobalt ion; and (C) *hs*-[$Co^{II}(SQ)_2$] with a ferromagnetic alignment of the spins of the cobalt and SQ^- ligands.

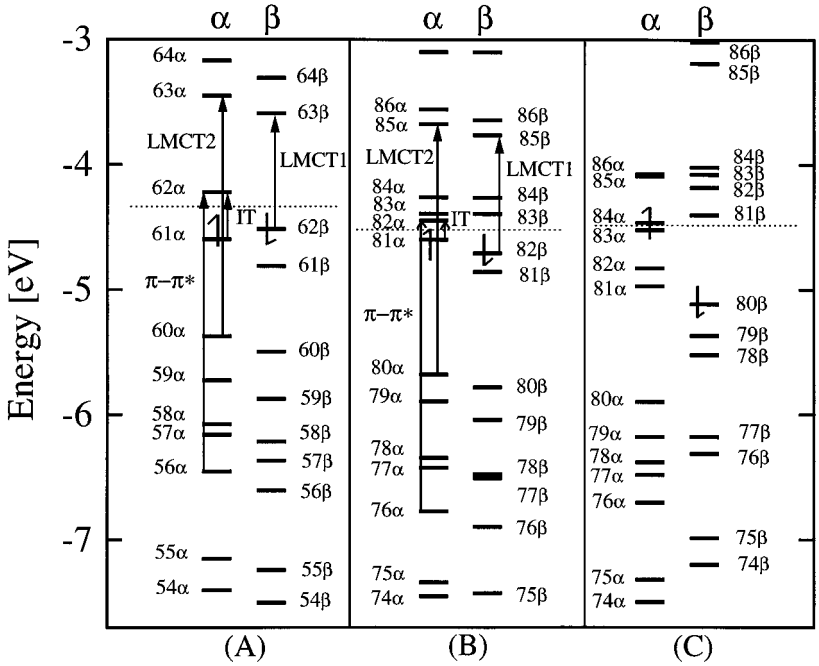

Figure 9. Molecular orbital energy level diagrams obtained from calculations utilizing a VBP potential for (A) *ls*-[Co^{III}(SQ)(Cat)(en)], (B) *ls*-[Co^{III}(SQ)(Cat)(phen)], and (C) *ls*-[$Co^{II}(SQ)_2$(phen)] (238 K structure) with a ferromagnetic alignment of the spins of the ligands and the cobalt ion. Some important electronic transitions have also been indicated.

description of the *hs*-[$Co^{II}(SQ)_2$] valence-tautomeric state which has the occupation scheme Co^{II} $d^5\alpha$ $d^2\beta$ ($S = {}^3/_2$), SQ_1 $\pi^{*1}\alpha$ $\pi^{*0}\beta$ ($S = {}^1/_2$), SQ_2 $\pi^{*1}\alpha$ $\pi^{*0}\beta$ ($S = {}^1/_2$). Here there is a relatively large energy splitting between majority α and minority β spin 3d energy levels and semiquinone π^* energy levels due to the increase in unpaired spin. Also, the ligand field splitting has been substantially reduced since the metal−ligand bond distances have increased by ∼0.2 Å in converting from the *ls*-Co^{III} to the *hs*-Co^{II} tautomer. The spin polarization energy slightly exceeds the ligand field stabilization energy, and consequently the competition favors a *high-spin* cobalt ion. The intermediate situation, *ls*-[$Co^{II}(SQ)_2$] shown in Figure 8B, has the occupation scheme Co^{II} $d^4\alpha$ $d^3\beta$ ($S = {}^1/_2$), SQ_1 $\pi^{*1}\alpha$ $\pi^{*0}\beta$ ($S = {}^1/_2$), SQ_2 $\pi^{*1}\alpha$ $\pi^{*0}\beta$ ($S = {}^1/_2$). In this case the spin polarization energy is smaller than the ligand field stabilization energy and the competition favors a *low-spin* cobalt ion. Simple MO pictures, such as extended Hückel, that ignore these spin polarization effects that result in energy splitting between majority and minority spin levels can lead to misleading descriptions of the balance of forces in high-spin transition metal complexes.

(C) *ls*-[Co^{III}(SQ)(Cat)(phen)] Electronic Structure. Figure 9B displays the molecular orbital energy level diagram of the *ls*-[Co^{III}(SQ)(Cat)(phen)] valence-tautomeric state obtained with a VBP exchange correlation potential. The orbital characters and gross populations of these molecular orbitals are available in Table 1; the parentages were obtained from a standard Mulliken population analysis. As a matter of convenience the ligand field set has been arbitrarily given the symmetry labels of O_h symmetry, even though the complex has no overall symmetry. The Fermi level is indicated by a dashed line, below which the orbitals are fully occupied, and above which lie the unoccupied virtual molecular orbitals. The unpaired electron has been arbitrarily assigned to a β spin orbital.

Table 1. Occupations, Molecular Orbital Energies, Mulliken Populations, and Molecular Orbital Characters Obtained from Calculations Utilizing a VBP Potential for *ls*-[Co^{III}(SQ)(Cat)(en)] and *ls*-[Co^{III}(SQ)(Cat) (phen)]

orbital	occupation	energy (eV)	percentage (%) Co	Cat^{2-}	SQ^{-}	N⌒N	character[a]
			(A) *ls*-[Co^{III}(SQ)(Cat)(en)]				
54α	1	−7.403	13.9	40.0	24.5		σ-Cat
55α	1	−7.152	11.6	29.2	40.4		σ-SQ
56α	1	−6.452	35.5	17.0	40.1		Co t_{2g}
57α	1	−6.159	34.8	21.2	34.2		Co t_{2g}, π-SQ
58α	1	−6.075	47.1	25.1	17.6		Co t_{2g}, π-Cat
59α	1	−5.727	53.4	13.2	23.0		Co t_{2g}, π-SQ
60α	1	−5.375	37.6	55.9	1.1		π-Cat, Co t_{2g}
61α	1	−4.597	3.6	60.1	25.5		π*-Cat, π*-SQ
62α	0	−4.221	15.3	25.5	53.1		π*-SQ, π*-Cat
63α	0	−3.450	61.1	7.1	14.0	10.9	Co e_g*
64α	0	−3.169	59.8	19.0	7.4	6.6	Co e_g*
54β	1	−7.503	20.1	42.4	17.3		σ-Cat, σ-SQ
55β	1	−7.242	12.6	34.9	36.3		σ-Cat, σ-SQ
56β	1	−6.603	42.5	17.6	30.5		Co t_{2g}, π-SQ
57β	1	−6.365	30.5	10.3	49.8		Co t_{2g}, π-SQ
58β	1	−6.214	40.8	32.0	15.9		Co t_{2g}, π-Cat
59β	1	−5.875	53.9	13.3	22.2		Co t_{2g}, π-SQ
60β	1	−5.499	34.8	59.2			π-Cat, Co t_{2g}
61β	1	−4.811	3.1	42.4	45.0		π*-Cat, π*-SQ
62β	1	−4.515	12.4	44.7	36.4		π*-SQ, π*-Cat
63β	0	−3.590	59.9	7.5	13.1	11.4	Co e_g*
64β	0	−3.307	59.0	19.6	7.5	7.8	Co e_g*
			(B) *ls*-[Co^{III}(SQ)(Cat)(phen)]				
74α	1	−7.452	15.5	31.6	32.7		σ-Cat, σ-SQ
75α	1	−7.341	15.9	29.2	39.2		σ-Cat, σ-SQ
76α	1	−6.771	58.1	21.2	17.4		Co t_{2g}, π-Cat
77α	1	−6.422	48.1	18.9	16.5		Co t_{2g}
78α	1	−6.344	50.1	29.6	16.8		Co t_{2g}, π-Cat
79α	1	−5.894	11.7	11.1	70.3		π-SQ
80α	1	−5.681	23.4	63.9	5.0		π-Cat, Co t_{2g}
81α	1	−4.599	1.8	60.3	31.9		π*-Cat, π*-SQ
82α	0	−4.446	8.2	29.8	57.8		π*-SQ, π*-Cat
83α	0	−4.393				100.0	π*-phen
84α	0	−4.261				100.0	π*-phen
85α	0	−3.675	58.8	7.2	14.6		Co e_g*
86α	0	−3.558	58.0	20.1	7.4	6.3	Co e_g*
75β	1	−7.427	16.5	30.9	36.3		σ-Cat, σ-SQ
76β	1	−6.895	59.2	19.2	16.3		Co t_{2g}
77β	1	−6.506	48.4	17.0	16.4		Co t_{2g}
78β	1	−6.474	45.4	20.5	21.1		Co t_{2g}
79β	1	−6.041	13.9	10.7	69.7		π-SQ
80β	1	−5.782	22.5	67.9			π-Cat, Co t_{2g}
81β	1	−4.858	2.8	23.4	70.0		π*-SQ, π*-Cat
82β	1	−4.710	7.8	66.8	18.8		π*-Cat, π*-SQ
83β	0	−4.392				100.0	π*-phen
84β	0	−4.265				100.0	π*-phen
85β	0	−3.764	58.4	7.5	14.4	9.2	Co e_g*
86β	0	−3.644	58.8	19.3	7.2	7.6	Co e_g*

[a] The notations indicate the dominate character(s) of each molecular orbital: σ-Cat and σ-SQ indicate dominance from σ catecholate and semiquinonate $9a_1$ and $7b_2$ orbitals; π-Cat and π-SQ indicate dominance from π catecholate and semiquinonate $2a_2$ orbitals; π*-Cat and π*-SQ indicate dominance from π* catecholate and semiquinonate $3b_1$ orbitals; Co t_{2g} and Co e^*_g for metal orbitals.

Comparison of the energy level structure in Figure 9B to the idealized energy level structure in Figure 8A leads one to quickly identify the ligand field split metal d levels, the $3b_1$ π* quinone orbitals, as well as the π* phenanthroline orbitals (shown in Figure 9B only). The t_{2g} set of the *ls*-Co^{III} ion ($d^3\alpha$ $d^3\beta$) is predominately distributed in orbitals 76α−78α and 76β−78β. However, some t_{2g} character is present in the orbitals 79−80 (α and β). The unoccupied e_g* set is composed of orbitals 85α−86α and 85β−86β. The ligand field splitting then is approximately 2.8 eV for both α and β spins, which is to be expected for a ligand field of four oxygen and two nitrogen atoms bonded to a Co^{III} ion. The unoccupied phenanthroline π* levels lie above the SQ^- and Cat^{2-} π* levels and remain essentially unmixed either with the cobalt ion or *o*-quinone ligands. There is only a slight spin-polarized exchange splitting between minority α and majority β spin levels. One extra electron is housed in the β manifold, and consequently we see a slight stabilization of the β spin levels and a slight destabilization of α spin levels. The idealized energy level structure in Figure 8A, however, shows the extra electron housed in the α manifold. This was done for illustrative purposes in Figure 8 in order to keep the excess spin in the α manifold across the series.

There is a substantial degree of mixing between the π* orbitals of the different *o*-quinone ligands. Previous to these calculations, *ls*-[Co^{III}(SQ)(Cat)] complexes were simply described as having ligands in different formal oxidation states, *i.e.*, either Cat^{2-} or SQ^-. This description was based primarily on X-ray structure determinations of internal ligand bond lengths, which show differences between Cat^{2-} and SQ^- ligands. The X-ray structural data for the [Co^{III}(SQ)(Cat)(phen)] complex studied in this work clearly show different bond lengths for the two *o*-quinone ligands, indicating Cat^{2-} and SQ^- groups. However, the calculations show that, even though there are trapped valences present for the two *o*-quinone-derived ligands bound to one cobalt ion, there are appreciable covalent interactions present. Covalent interactions between the cobalt ion and its ligands lead to molecular orbitals that simultaneously have contributions from both "Cat^{2-}" and "SQ^-" ligands. For example, in Figure 9B, orbitals 81α−82α and 81β−82β are the $3b_1$ π* orbitals of the catecholate and semiquinonate ligands. The occupied orbitals 81α and 82β correspond to the occupied $3b_1$ π* orbital of the catecholate ligand having, respectively, 60.3% and 66.8% π* Cat^{2-} character. However, the π* SQ^- orbital contributes 31.9% and 18.8% to these molecular orbitals, respectively. Orbital 81β is the occupied $3b_1$ π* SQ^- magnetic orbital, and orbital 82α is its unoccupied partner. The magnetic orbital 81β has 70.0% π* SQ^- character and 23.4% π* Cat^{2-} character, which indicates that the unpaired spin density is predominately located on the SQ^- moiety, but with significant leakage onto the Cat^{2-} ligand. It should be noted that these results show that the major contributor to the magnetic orbital is the SQ^- ligand, which is in agreement with that identified by X-ray analysis; however, substantial unpaired spin density is also located over the ring of the Cat^{2-} ligand.

The electronic transition marked by IT in Figure 9B represents the intervalence charge transfer transition between the mixed-valent Cat^{2-}/SQ^- pair. The Cat^{2-}/SQ^- pair is an asymmetric mixed-valence pair, since there exists a clear structural difference between the two *o*-quinone ligands in the *ls*-[Co^{III}(SQ)(Cat)-(phen)] crystal structure. Orbital 81α is the highest occupied molecular orbital (HOMO) and is predominately (60.3%) the $3b_1$ π* orbital of the Cat^{2-} ligand. Orbital 82α is the lowest unoccupied molecular orbital (LUMO) and is largely (57.8%) the $3b_1$ π* orbital of the SQ^- ligand. The lowest energy transition results in transfer of charge between the Cat^{2-} and SQ^- ligands.

(D) Cobalt *o*-Quinone Bonding. Figure 10 shows orbital isovalue contour diagrams of the important *o*-quinone metal interactions. The view is of the catecholate ligand (C2−C7, O2, and O7) and cobalt atom in the *YZ*-plane. Figure 10A is an illustrative diagram showing the orientation of the Cat^{2-} ring, the axis system, and the slicing planes. Although we have chosen to show only the contours of the catecholate ligand interacting with the cobalt, the interactions are representative of *o*-quinone−metal interactions and can be used to understand

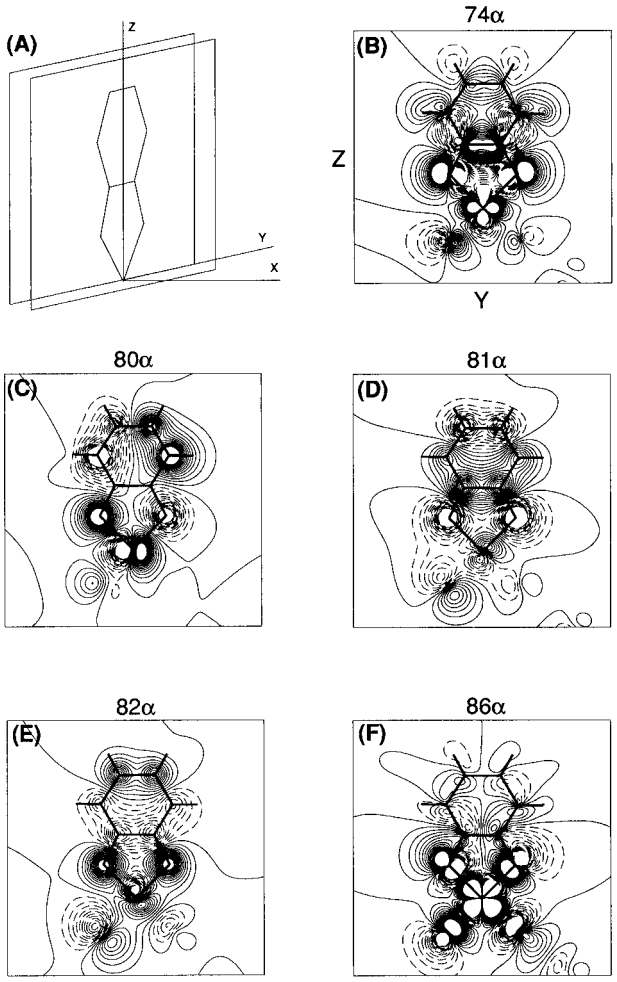

Figure 10. Molecular orbital isovalue contour plots displaying the important cobalt *o*-quinone orbital interactions. The plots are of particular molecular orbitals of the *ls*-[Co^{III}(SQ) (Cat)(phen)] complex. (A) Illustrative diagram showing the orientation of the *o*-quinone ring, the axis system, and the slicing planes. (B,F) Orbitals 74α and 86α involve σ type interactions and are pictured as slices through the plane of the ring. (C−E) Molecular orbitals 80α, 81α, and 82α, respectively, are π type orbitals and were obtained as slices 0.5 Å above the plane of the ring in the positive *x*-direction.

the essential features of all of the calculations presented here. Slices have been taken through the plane of the ring for orbitals 74α and 86α and at a distance of 0.5 Å above the plane of the ring for orbitals 80α−82α, as illustrated in Figure 10A.

Molecular orbitals 74−75 (α and β) correspond to the $9a_1$ orbitals of the Cat^{2-} and SQ^- ligands interacting with the metal in a bent σ-bonding fashion. The isovalue contour plot, Figure 10B, of orbital 74α sliced through the plane of the catecholate ring clearly reveals the $9a_1$ Cat^{2-} symmetric combination of p orbitals at the oxygen atoms interacting with the predominately d_{z^2} atomic orbital at the cobalt. Orbital 74α has 31.6% Cat^{2-} ($9a_1$), 32.7% SQ^- ($9a_1$), and 15.5% metal σ character. It can also be seen in Figure 10B that molecular orbital 74α is largely localized on the p orbitals of the Cat^{2-} and SQ^- ligands and metal d_{z^2} atomic orbital.

Molecular orbitals 85−86 (α and β) are the e_g* antibonding orbitals of the ligand field set. Figure 10F displays the isovalue contour plot of orbital 86α taken as a slice through the plane of the catecholate ring. Orbital 86α is composed of 58% cobalt d_{yz} and 20.1% Cat^{2-} ($7b_2$). Figure 10F illustrates the σ-antibonding interaction of the metal d_{yz} orbital with the antisymmetric combination of p orbitals of the Cat^{2-} ($7b_2$) orbital. The 86α orbital is localized predominately on the metal d_{yz} orbital and the antisymmetric combination of p orbitals at the oxygen atoms, but also reflects some σ-antibonding interactions between the cobalt ion and the other ligands.

Orbitals 79−80 (α and β) and 81−82 (α and β) represent metal−ligand π interactions. Contours of these π-type orbitals have been taken at a distance of 0.5 Å above the plane of the ring in order to capture the nodal pattern of the p_x orbitals of the catecholate interacting with the metal π orbitals. Orbital 80α, Figure 10F, is a π-antibonding interaction between the catecholate $2a_2$ π molecular orbital and the cobalt d_{xy} orbital in a "side on" fashion. This orbital is largely localized at the cobalt in the d_{xy} orbital (23.4%) and delocalized over the p_x framework of the catecholate ring (63.9%). Orbital 80α is representative of the metal−ligand interactions found in orbitals 79−80 (α and β). The $3b_1$ π* orbitals of the semiquinonate and catecholate ligands are located in orbitals 81−82 (α and β). Contour plots, Figure 10D,E, of molecular orbitals 81α and 82α display the π-antibonding interaction between the π* $3b_1$ orbital of the catecholate ligand and the metal d_{xz} orbital. Orbitals 81α and 82β are the HOMOs associated with the filled $3b_1$ π* orbital of the catecholate ligand. Orbital 81β is the magnetic orbital largely associated with the SQ, which holds most of the unpaired β spin density. Orbital 82α is the unoccupied $3b_1$ π* counterpart of magnetic orbital 81β. This unoccupied orbital 82α is composed of 8.2% cobalt t_{2g}, 57.8% SQ^- π*, and 29.8% Cat^{2-} and resembles the net distribution of spin density throughout the molecule. Orbitals 76−78 (α and β) represent predominately the cobalt t_{2g} set, but also contain contributions from the $2a_2$ π orbitals, as well as lower lying π orbitals of the *o*-quinone ligands.

(E) *ls*-[Co^{III}(SQ)(Cat)(en)] Electronic Structure. This complex is analogous to *ls*-[Co^{III}(SQ)(Cat)(phen)], except that the saturated en ligand does not have any π* orbitals close to the highest occupied molecular orbitals. This electronic structure calculation was initially undertaken in order to compare the structures of valence-tautomeric complexes with and without the π* orbitals of the counter ligand present. In this way it is possible to understand the influence of the counter-ligand on the valence-tautomeric interconversion. Moreover, it was found that calculating electronic transitions in such a complex without π* orbitals greatly simplified the results of these calculations.

Figure 9A shows the molecular orbital energy diagram calculated for *ls*-[Co^{III}(SQ)(Cat)(en)] employing a VBP exchange correlation potential. Table 1 lists the Mulliken gross populations of the molecular orbitals of this complex. Again comparing this molecular orbital level diagram to the qualitative diagram in Figure 8A we can quickly identify the ligand field split metal d levels and the $3b_1$ π* quinone molecular orbitals. The t_{2g} set is essentially spread over orbitals 56−60 (α and β) due to π-type interactions with the Cat^{2-} and SQ^- ligands. Orbitals 59−60 (α and β) reflect the antibonding interactions of the Cat^{2-} and SQ^- $2a_2$ orbitals with the metal t_{2g} in a manner exactly analogous to that shown in Figure 10C. The unoccupied e_g* set is found in orbitals 63−64 (α and β). The ligand field splitting (10 Dq) for the en complex was calculated to be 2.64 eV, which is slightly less than the splitting of 2.77 eV calculated for the *ls*-Co^{III} phenanthroline complex. As expected, the spin-polarized exchange splitting between minority α and majority β spin levels is similar to that found in the phen complex. One extra electron is housed in the β manifold, and we see a slight stabilization of 0.147 eV of the β spin levels and a corresponding destabilization of the α spin levels.

The $3b_1$ π* orbitals of the Cat^{2-} and SQ^- ligands are found in orbitals 61−62 (α and β) and are again mixed in a fashion similar to that found for the phen complex. Orbital 61α and

62β are predominately Cat^{2-} in nature and correspond to the occupied $3b_1$ π* orbital. Orbital 61β is the occupied magnetic orbital containing most of the unpaired spin density and whose major contribution is from the π* orbital of the SQ^- (45.0%) ligand. Orbital 62α is the unoccupied π* partner of the magnetic orbital containing 53.1% π* SQ^-, 25.5% π* Cat^{2-}, and 15.3% Co t_{2g} character. Unfilled orbital 62α represents in character the net distribution of unpaired spin which is located in β. It is important to note that the major contributor to the magnetic orbital is the SQ^- ligand, which is in agreement with the SQ^- ligand identified in the X-ray structure report.[9b]

(F) Spin-Aligned *ls*-[$Co^{II}(SQ)_2$(phen)] Electronic Structure. The calculation of the electronic structure for either the *hs*-[$Co^{II}(SQ)_2$(phen)] or *ls*-[$Co^{II}(SQ)_2$(phen)] valence tautomers is not as straightforward as for the *ls*-[Co^{III}(SQ)(Cat)(phen)] tautomer. In the case of the Co^{II} complexes there are magnetic exchange interactions present between the metal unpaired electrons and the unpaired electrons on the semiquinonate ligands. For *hs*-[$Co^{II}(SQ)_2$(phen)] the exchange interactions between the $S = {}^3/_2$ Co^{II} ion and the two $S = {}^1/_2$ SQ^- ligands give rise to four different electronic states: one $S = {}^1/_2$ spin state where the cobalt spin is aligned antiparallel to the spins on each of the SQ^- ligands, two $S = {}^3/_2$ states, and one $S = {}^5/_2$ state where the $S = {}^3/_2$ spin of the Co^{II} ion is aligned parallel to both $S = {}^1/_2$ SQ^- spins. This assumes that both Co−SQ interactions have equal exchange parameters (J in $\hat{H} = -2J\hat{S}_{Co}\cdot\hat{S}_{SQ}$ for each Co−SQ interaction). In short, in order to characterize the electronic structure of the lowest states for the *hs*-[$Co^{II}(SQ)_2$(phen)] complex it is necessary to determine the electronic structure for the four spin states that comprise the $S = {}^1/_2$, ${}^3/_2$, ${}^3/_2$, ${}^5/_2$ spin ladder of this Co^{II} complex. This is done by calculating the electronic structure for the spin-aligned $S = {}^5/_2$ spin state for this *hs*-Co^{II} complex. The energetics and wavefunctions of the other ($S = {}^1/_2$ and two $S = {}^3/_2$) states are determined by carrying out the same type of calculation for a broken symmetry (BS) state to determine the exchange parameter J for the complex (*vide supra*).

In the case of the hypothetical *ls*-[$Co^{II}(SQ)_2$(phen)] complex the magnetic exchange interactions between the low-spin $S = {}^1/_2$ Co^{II} ion and the two $S = {}^1/_2$ SQ^- ligands give two $S = {}^1/_2$ spin states and one $S = {}^3/_2$ state where the cobalt spin is aligned parallel to the spins on the two SQ^- ligands. The energy and wavefunction of the $S = {}^1/_2$ spin states can be evaluated by a calculation for a broken symmetry state (*vide infra*). In this section are given the results for the spin-aligned $S = {}^3/_2$ spin state for *ls*-[$Co^{II}(SQ)_2$(phen)].

Figure 9C displays the molecular orbital energy level diagram for the spin-aligned *ls*-Co^{II} state. Table 2 lists in greater detail the Mulliken gross populations of the molecular orbitals. Although this complex should be somewhat Jahn−Teller distorted, the crystal structure showed no evidence of such an effect. Consequently, a near degeneracy exists in the e_g* orbitals 83α and 84α which house the single unpaired electron of the *ls*-Co^{II} center. In order to achieve convergence in this calculation, a Slater transition state approach was invoked that places 0.5 of an electron in each of the near degenerate orbitals. After convergence, the energy separation of 0.059 eV (476 cm^{-1}) between these orbitals is the energy separation between these nearly degenerate states.

The idealized spin-polarized ligand field diagram of Figure 8B is useful for understanding the calculated molecular orbital diagram of Figure 9C. The *ls*-Co^{III} to *ls*-Co^{II} transformation has increased the metal−ligand bond lengths by ∼0.1 Å, and consequently, the average ligand field splitting has decreased from ∼2.8 eV to ∼2.0 eV. The spin polarization splitting between the majority α and minority β levels is ∼1.3 eV, which is still less than the ligand field splitting, and consequently the *ls*-Co^{II} description is favored. The t_{2g} set in the α spin manifold is substantially mixed with the $2a_2$ π molecular orbitals of the semiquinonates. However, due to spin polarization destabilization of minority β levels, the t_{2g} orbitals 78β−80β are raised in energy and have much less mixing with the π SQ^- orbitals. Orbitals 81α and 82α are the occupied SQ $3b_1$ π* magnetic

Table 2. Occupations, Molecular Orbital Energies, Mulliken Populations, and Molecular Orbital Characters Obtained from Calculations Utilizing a VBP Potential for *ls*-[$Co^{II}(SQ)_2$(phen)] (238 K X-ray Structure) with Ferromagnetically Aligned Spins and the Broken Symmetry *ls*-[$Co^{II}(SQ)_2$(phen)] (238 K X-ray Structure)

orbital	occupation	energy (eV)	percentage (%) Co	SQ_1	SQ_2	phen	character[a]
			(A) *ls*-[$Co^{II}(SQ)_2$(phen)][b]				
75α	1	−7.321	25.1	20.9	33.9		σ-SQ
76α	1	−6.702	44.3	21.8	25.9		Co t_{2g}, π-SQ
77α	1	−6.479	19.6	39.5	29.8		Co t_{2g}, π-SQ
78α	1	−6.378	35.4	20.9	32.2		Co t_{2g}, π-SQ
79α	1	−6.177	41.3	24.7	23.2		Co t_{2g}, π-SQ
80α	1	−5.898	65.1	16.7	9.4		Co t_{2g}, π-SQ
81α	1	−4.971	4.3	83.7	1.4		π*-SQ
82α	1	−4.828	8.8	4.6	81.5		π*-SQ
83α	0.5	−4.522	56.8	11.3	7.9	11.6	Co e_g*
84α	0.5	−4.463	60.0	11.8	14.6	3.1	Co e_g*
85α	0	−4.091				100.0	π*-phen
86α	0	−4.074				100.0	π*-phen
75β	1	−6.986	13.4	14.0	53.2		σ-SQ
76β	1	−6.310	10.1	37.7	47.1		π-SQ
77β	1	−6.177	1.6	35.8	41.6		π-SQ
78β	1	−5.526	57.7	18.5	13.3		Co t_{2g}, π-SQ
79β	1	−5.372	61.6	12.0	10.2		Co t_{2g}, π-SQ
80β	1	−5.115	80.2	4.8	3.2		Co t_{2g}
81β	0	−4.402	7.8	61.0	19.1		π*-SQ
82β	0	−4.185	18.6	16.5	54.5		π*-SQ
83β	0	−4.078	4.4			93.6	π*-phen
84β	0	−4.022	10.0			88.3	π*-phen
85β	0	−3.190	72.4	7.6	10.2	1.8	Co e_g*
86β	0	−3.019	73.6	6.7	3.7	8.8	Co e_g*
			(B) *ls*-[$Co^{II}(SQ)_2$(phen)][c]				
75α	1	−7.306	22.2	33.2	27.3		σ-SQ
76α	1	−6.554	37.4	16.2	42.0		Co t_{2g}, π-SQ
77α	1	−6.340	21.2	39.5	29.7		Co t_{2g}, π-SQ
78α	1	−6.232	47.1	17.9	24.8		Co t_{2g}, π-SQ
79α	1	−5.990	45.4	27.0	14.3		Co t_{2g}, π-SQ
80α	1	−5.782	61.0	23.2	6.8		Co t_{2g}, π-SQ
81α	1	−4.802	3.5	37.9	50.8		π*-SQ
82α	1	−4.697	8.6	53.5	31.3		π*-SQ
83α	0	−4.263	9.2			89.5	π*-phen, Co t_{2g}
84α	0	−4.241				100.0	π*-phen
85α	0	−4.186	59.6	10.1	10.9	4.1	Co e_g*
86α	0	−3.908	68.6	8.7	4.4	10.0	Co e_g*
75β	1	−7.238	24.4	27.0	28.2		Co e_g, σ-SQ
76β	1	−6.523	52.2	12.0	25.7		Co t_{2g}, π-SQ
77β	1	−6.327	40.7	23.4	19.7		Co t_{2g}, π-SQ
78β	1	−6.189	47.6	11.9	26.6		Co t_{2g}, π-SQ
79β	1	−5.967	24.2	29.7	41.5		Co t_{2g}, π-SQ
80β	1	−5.779	39.3	44.2	8.9		Co t_{2g}, π-SQ
81β	1	−4.512	22.0	37.3	26.2	3.1	Co e_g, π*-SQ
82β	0	−4.411	22.2	51.4	8.5	1.5	π*-SQ_1, Co e_g*
83β	0	−4.351	18.9	1.8	49.5	8.8	π*-SQ_2, Co e_g*
84α	0	−4.324	65.5	14.7	10.4	1.2	Co e_g*, σ-SQ
85β	0	−4.243	7.8		1.6	88.4	π*-phen
86β	0	−4.239	5.2			92.1	π*-phen

[a] The notations indicate the dominate character(s) of each molecular orbital: σ-Cat and σ-SQ indicate dominance from σ catecholate and semiquinonate orbitals; π-Cat and π-SQ indicate dominance from π catecholate and semiquinonate orbitals; π*-Cat and π*-SQ indicate dominance from π* catecholate and semiquinonate orbitals; Co t_{2g} and Co e*$_g$ for metal orbitals. [b] Low-spin d^7 cobalt $S = {}^1/_2$, two $S = {}^1/_2$ SQ^- ferromagnetically aligned. [c] Low-spin d^7 cobalt with two $S = {}^1/_2$ SQ^- antiferromagnetically aligned (BS).

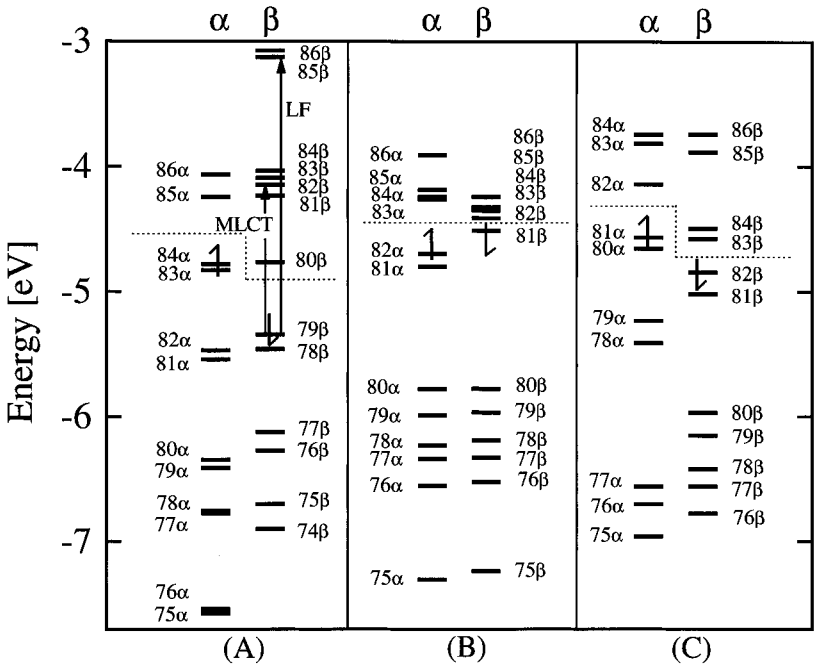

Figure 11. Molecular orbital energy level diagrams obtained from calculations utilizing a VBP potential for (A) *hs*-[$Co^{II}(SQ)_2$(phen)] (300 K structure) with a ferromagnetic alignment of the spins associated with the ligands and cobalt ion and the broken symmetry states calculated using a VBP potential; (B) BS *ls*-[$Co^{II}(SQ)_2$(phen)] (238 K structure) with an antiferromagnetic alignment of the spins of the ligands and the cobalt ion; and (C) BS *hs*-[$Co^{II}(SQ)_2$(phen)] (300 K structure) with an antiferromagnetic alignment of spins of the ligands and cobalt ion. Some important electronic transitions are also indicated.

orbitals and remain largely unmixed with each other. This is in contrast to the delocalization which occurs between the SQ^- and Cat^{2-} π^* orbitals of the *ls*-Co^{III} tautomer. The single unpaired electron of the cobalt ion occupies the nearly degenerate e_g^* orbitals 83α and 84α. These orbitals are now energetically closer to the SQ π^* orbitals 81α and 82α compared to the e_g^* orbitals in the *ls*-Co^{III} complex.

(G) Spin-Aligned *hs*-[$Co^{II}(SQ)_2$(phen)] Electronic Structure. Figure 11A shows the molecular orbital energy diagram for the *hs*-[$Co^{II}(SQ)_2$(phen)] valence-tautomeric system, obtained with a VBP exchange correlation potential. This diagram can be interpreted with the aid of Figure 8C. Table 3 lists the gross Mulliken populations of the molecular orbitals. Since this molecule has five unpaired electrons, the majority α spin cobalt ligand field and SQ^- π^* levels are substantially stabilized in energy relative to the minority β spin levels. The spin polarization splitting of ∼2.4 eV exceeds the ligand field splitting of ∼2.0 eV, and consequently, the *hs*-Co^{II} description is favored. The α spin t_{2g} 74α−76α orbitals are greatly lowered in energy to ∼−7.5 eV. The cobalt e_g antibonding magnetic orbital set 81α−82α are lower in energy than the SQ^- $3b_1$ π^* magnetic orbitals 83α−84α. The magnetic $3b_1$ π^* orbitals 83α and 84α have a very localized character and remain essentially unmixed with each other and the cobalt orbitals. However, the unoccupied β spin $3b_1$ π^* orbitals are destabilized in energy due to spin polarization effects and are substantially mixed with the phen π^* orbitals (81β−84β). Furthermore, these orbitals contain contributions (8.4−14.6%) from the metal t_{2g} orbitals. Two sets of electronic transitions are marked which originate in the highest occupied minority spin t_{2g} levels and involve excitation to the ligand π^*(MLCT) and e_g^*(LF) orbitals.

Spin polarization splitting raises the energy of β minority spin t_{2g} levels to lie closer in energy to the ligand π^* orbitals. Consequently, back-bonding develops between the t_{2g} orbitals 78β−80β and the unoccupied π^* orbitals 81β−84β. The occupied orbitals 78β and 79β contain contributions of 64.8% and 63.8%, respectively, from the t_{2g} orbitals. In addition, the $3b_1$ π^* orbitals contribute 26.0% and 14.9%, respectively, to these same orbitals. On the other hand, the π^* orbitals 82β−84β contain from 8.4 to 14.6% cobalt t_{2g} contribution. The occupied metal t_{2g} orbitals are stabilized at the expense of the unoccupied ligand π^* orbitals. This ultimately serves to lower the total bonding energy and increase the observed ligand field splitting. The same back-bonding situation is also evident in the *ls*-Co^{II} system in the t_{2g} 78β−80β and SQ^- π^* 81β−82β orbitals.

(H) Broken Symmetry States. Spin-unrestricted density functional calculations in broken symmetry (BS) were performed in order to determine the exchange parameter J (in $\hat{H} = -2\sum_{i>j}J_{ij}S_i \cdot S_j$) that characterizes the magnetic exchange interaction between the semiquinonate ligands and Co^{II} ions of the *hs*-[$Co^{II}(SQ)_2$] and *ls*-[$Co^{II}(SQ)_2$] valence tautomers. The complete details of the broken symmetry formalism and its application to magnetic exchange coupling in polynuclear metal complexes have been published elsewhere.[40,41] Computationally it is difficult to represent pure spin states of a spin-coupled system within density functional theory. However, calculation of the eigenfunction and eigenvalue of the broken symmetry state is straightforward. The antiferromagnetic state of a spin-coupled system in density functional theory is represented by a "broken symmetry" state. In practice, the charge density α and β fit coefficients from the converged ferromagnetic *high-spin* calculation are interchanged on one (or two) of the spin-coupled atoms and used as a starting point for the calculation of the broken symmetry state. A broken symmetry state is a single determinantal wavefunction. The BS state in an exchange-coupled complex can be described as a linear combination of pure spin states. The precise composition of a broken symmetry state can be computed and the magnetic exchange coupling parameters J can be determined from the differences in energy between the broken and high-spin symmetry states.

The antiferromagnetic $M_s = {}^1/_2$ broken symmetry *hs*-[Co^{II}-$(SQ)_2$(phen)] state is constructed by aligning the net spin density

(40) Noodleman, L.; Case, D. A. *Adv. Inorg. Chem.* **1992**, *38*, 423.
(41) Noodleman, L.; Baerends, E. J. *J. Am. Chem. Soc.* **1984**, *106*, 2316.

Table 3. Occupations, Molecular Orbital Energies, Mulliken Populations, and Molecular Orbital Characters Obtained from Calculations Utilizing a VBP Potential for *hs*-[$Co^{II}(SQ)_2$(phen)] (300 K X-ray Structure) Ferromagnetically Aligned and Broken Symmetry *hs*-[$Co^{II}(SQ)_2$(phen)] (300 K X-ray Structure)

orbital	occupation	energy (eV)	percentage (%) Co	SQ_1	SQ_2	phen	character[a]
			(A) *hs*-[$Co^{II}(SQ)_2$(phen)][b]				
75α	1	−7.576	47.2	7.6	19.0	6.4	Co t_{2g}
76α	1	−7.540	56.0	13.1	10.8	1.4	Co t_{2g}
77α	1	−6.772	20.1	12.6	49.4	1.2	σ-SQ
78α	1	−6.754	25.0	43.0	12.6		σ-SQ
79α	1	−6.410	2.4		92.0		π-SQ
80α	1	−6.345	1.7	96.2			π-SQ
81α	1	−5.545	43.5	22.4	14.7	6.9	Co e_g*
82α	1	−5.472	39.3	12.8	19.3	9.4	Co e_g*
83α	1	−4.828	1.7	89.9	1.4		π*-SQ
84α	1	−4.780	3.2	3.6	88.5		π*-SQ
85α	0	−4.244				100.0	π*-phen
86α	0	−4.065				100.0	π*-phen
75β	1	−6.699	16.2	41.1	24.1		
76β	1	−6.271	6.8	12.0	75.6		
77β	1	−6.123	1.8	76.6	13.0		
78β	1	−5.463	64.8	12.9	13.1		Co t_{2g}
79β	1	−5.345	63.8	8.7	6.2		Co t_{2g}
80β	0	−4.764	83.9	1.2	1.8		Co t_{2g}
81β	0	−4.233		38.5	12.7	43.1	π*-phen, π*-SQ
82β	0	−4.146	14.6	12.4	14.6	47.4	π*-phen, π*-SQ
83β	0	−4.090	8.4	25.8	14.7	44.3	π*-phen, π*-SQ
84β	0	−4.035	13.2	3.8	23.5	49.2	π*-phen, π*-SQ
85β	0	−3.125	71.3	6.2	2.9	8.3	Co e_g*
86β	0	−3.073	71.3	5.7	10.0	4.0	Co e_g*
			(B) *hs*-[$Co^{II}(SQ)_2$(phen)][c]				
75α	1	−6.960	8.5	48.2	24.8		
76α	1	−6.700	1.4	5.7	85.5		π-SQ_2
77α	1	−6.560		85.6	1.6		π-SQ_1
78α	1	−5.414	28.1	39.3	28.6		π*-SQ
79α	1	−5.235	24.0	26.9	36.4		π*-SQ
80α	1	−4.654	84.3	1.3	2.4		Co t_{2g}
81α	1	−4.566	46.9	24.4	5.7	4.5	Co t_{2g}, π*-SQ
82α	0	−4.140	62.8	5.6	12.2		Co t_{2g}, π*-SQ
83α	0	−3.816	13.2			86.8	π*-phen
84α	0	−3.744	6.4			93.7	π*-phen
85α	0	−2.634	79.2	7.1	3.8	3.5	Co e_g*
86α	0	−2.541	15.9			84.1	π*-phen
87α	0	−2.523	65.6		3.4	20.5	Co e_g*
76β	1	−6.775	38.3	12.0	37.9		Co t_{2g}, π-SQ
77β	1	−6.560	19.2	22.2	43.3		Co t_{2g}, π-SQ
78β	1	−6.420	10.4	66.0	12.2		Co t_{2g}, π-SQ
79β	1	−6.150	51.2	11.4	21.7		Co t_{2g}, π-SQ
80β	1	−5.970	61.2	22.0	9.8		Co t_{2g}, π-SQ
81β	1	−5.019	53.4	19.3	10.2	7.3	Co e_g*, σ-SQ
82β	1	−4.846	51.1	4.7	20.9	10.6	Co e_g*, σ-SQ
83β	0	−4.576	5.6		89.9		π*-SQ, Co t_{2g}
84β	0	−4.494	3.6	95.6			π*-SQ, Co t_{2g}
85β	0	−3.885				100.0	π*-phen
86β	0	−3.743				100.0	π*-phen

[a] The notations indicate the dominate character(s) of each molecular orbital: σ-Cat and σ-SQ indicate dominance from σ catecholate and semiquinonate $9a_1$ orbitals; π-Cat and π-SQ indicate dominance from π catecholate and semiquinonate $2a_2$ orbitals; π*-Cat and π*-SQ indicate dominance from antibonding π* and semiquinonate $3b_1$ orbitals; Co t_{2g} and Co e*$_g$ for metal orbitals. [b] High-spin d^7 cobalt with two $S = {}^1/_2$ SQ^- ferromagnetically aligned. [c] High-spin d^7 cobalt with two $S = {}^1/_2$ SQ^- antiferromagnetically aligned (BS).

of the *hs*-Co^{II} ion antiparallel to the net spin density of each of the semiquinonate ligands. Figure 12 and Chart 1 show the idealized spin-polarized ligand field diagrams and orbital occupations appropriate for the Co^{II} broken symmetry states and the Co^{III} state. Figure 12C displays the idealized energy level ordering evaluated for the ($M_s = -{}^1/_2$) BS *hs*-[$Co^{II}(SQ)_2$(phen)] state that has the occupation scheme *hs*-Co^{II} $d^2\alpha$ $d^5\beta$ ($S = {}^3/_2$), SQ_1 $\pi^{*1}\alpha$ $\pi^{*0}\beta$ ($S = {}^1/_2$), SQ_2 $\pi^{*1}\alpha$ $\pi^{*0}\beta$ ($S = {}^1/_2$). A comparison of this occupation scheme to the spin-aligned case shows that the spin indices α and β at the Co^{II} ion have been interchanged. While this broken symmetry state resembles the pure $S = {}^1/_2$ spin state, it also contains an admixture of pure spin states with $S \geq {}^1/_2$. In a similar fashion, flipping the spin at the *ls*-Co^{II} ion results in the antiferromagnetic $M_s = {}^1/_2$ BS *ls*-[$Co^{II}(SQ)_2$(phen)] state that has the occupation scheme *ls*-Co^{II} $d^3\alpha$ $d^4\beta$ ($S = {}^1/_2$), SQ_1 $\pi^{*1}\alpha$ $\pi^{*0}\beta$ ($S = {}^1/_2$), SQ_2 $\pi^{*1}\alpha$ $\pi^{*0}\beta$ ($S = {}^1/_2$). Likewise, this BS state resembles the pure $S = {}^1/_2$ state but it contains an admixture of pure $S \geq {}^1/_2$ spin states. The qualitative spin-polarized ligand field diagram for this broken symmetry state is shown in Figure 12B.

(I) BS *ls*-[$Co^{II}(SQ)_2$(phen)] Electronic Structure. Figure 11B and Table 2 give the molecular orbitals and detailed Mulliken populations calculated for the BS *ls*-Co^{II} state. The electronic structure of this BS *ls*-Co^{II} state closely resembles that of the *ls*-Co^{III} state, except that the energy of the e_g* orbitals has decreased since the metal ligand bond lengths have increased. Consequently, the $3b_1$ π* levels in the β spin manifold are nearly equal in energy to the cobalt e_g* orbitals. This results in considerable mixing in orbitals 81β−83β. Orbital 81β is the highly delocalized HOMO magnetic orbital composed of 22.0% e_g*, 37.3% SQ_1, and 26.2% SQ_2. The SQ^- contributions are predominately from $3b_1$ π* type molecular orbitals; however, some contribution is from the $7b_2$ σ molecular orbitals. Unoccupied orbitals 82β and 83β are also highly mixed, containing 51.4% SQ_1 π*/22.2% cobalt e_g* and 49.5% SQ_2 π*/18.9% cobalt e_g*, respectively. Orbitals 81α and 82α are the α spin SQ $3b_1$ π* magnetic orbitals which are antiferromagnetically coupled to β spin magnetic orbital 81β. The lowering of the e_g* orbitals in the *ls*-Co^{III} to *ls*-Co^{II} conversion has effectively resulted in transfer of some of the electron density from the Cat^{2-} π* orbital to the cobalt e_g* orbitals. Further stabilization of e_g* orbitals will ultimately result in complete electron transfer.

(J) BS *hs*-[$Co^{II}(SQ)_2$(phen)] Electronic Structure. The molecular orbital energy level structure and detailed Mulliken populations of the BS *hs*-Co^{II} state are shown in Figure 11C and Table 3, respectively. A comparison of the energy level structure of the BS *hs*-Co^{II} to that of spin-aligned *hs*-Co^{II} state reveals that spins at the cobalt have been interchanged. The minority α spin cobalt t_{2g} orbitals 80α−82α are energetically sandwiched between magnetic $3b_1$ π* SQ^- orbitals 78α−79α and π* phen orbitals 83α−84α. This corresponds to a back-bonding situation where the energy of the cobalt t_{2g} levels is modulated by the phen and SQ^- π* orbitals. The t_{2g} levels are stabilized in energy at the expense of the unoccupied phen π* levels. Conversely, the SQ^- π* orbitals are stabilized at the expense of destabilizing the t_{2g} levels. In fact, competing back-bonding interactions are present simultaneously in HOMO 81α. HOMO 81α is composed of 46.9% cobalt t_{2g}, 24.4% π* SQ_1, 5.7% π* SQ_2, and 4.5% π* phen. Larger counter-ligand π* back-bonding interactions would serve to lower the energy of the HOMO, while larger interactions with the SQ^- π* orbitals would serve to raise the energy of the HOMO.

(K) Charges and Net Spin Distributions. The oxidation states of the metal and the ligands are often of primary interest in the chemistry of transition metal complexes of *o*-quinones.[3] Formal oxidation states are often assigned to metal and ligands. However, the actual charge and spin distributions generally differ from these idealized oxidation states. In order to understand the metal−ligand charge and spin distributions in these complexes we have performed a Mulliken type population analysis on the results of our calculations. Tables 4 and 5 list

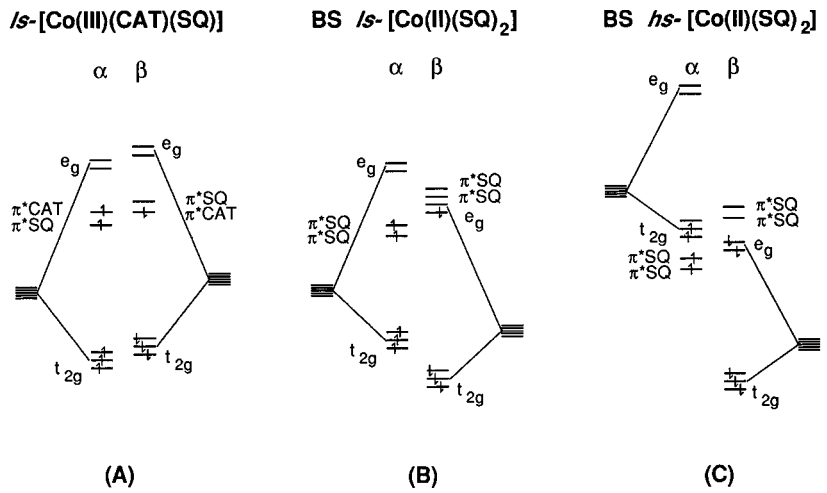

Figure 12. Idealized spin-unrestricted energy level diagrams of some important valence-tautomeric states showing the relative ordering of α spin and β spin energy levels of the ligand field set (O_h symmetry notation) and π^* orbitals of the *o*-quinone ligands: (A) *ls*-[Co^{III}(SQ)(Cat)]; (B) broken symmetry (BS) *ls*-[$Co^{II}(SQ)_2$] with an antiferromagnetic alignment of the spins of the ligands and the cobalt ion; and (C) broken symmetry (BS) *hs*-[$Co^{II}(SQ)_2$] with an antiferromagnetic alignment of the spins of the cobalt ion and the ligands.

Table 4. Net Spin Densities of Fragments of the Various Valence Tautomers Obtained for Calculations Which Utilized VBP and Xα Potentials

		net spin			
complex	potential	Co	Cat(SQ_1)	SQ_2	N⌒N
hs-[$Co^{II}(SQ)_2$(phen)] 300 K (cobalt $S = {}^3/_2$, two $S = {}^1/_2$ SQ^- ferromagnetically aligned)	VBP	2.719	1.102	1.108	0.074
	Xα	2.739	1.123	1.116	0.000
hs-[$Co^{II}(SQ)_2$(phen)] 300 K (cobalt $S = {}^3/_2$, two $S = {}^1/_2$ SQ^- antiferromagnetically aligned)	VBP	−2.313	0.753	0.429	0.117
	Xα	−2.398	0.705	0.605	0.088
ls-[$Co^{II}(SQ)_2$(phen)] 238 K (cobalt $S = {}^1/_2$, two $S = {}^1/_2$ SQ^- ferromagnetically aligned)	VBP	1.276	0.850	0.853	0.027
	Xα				
ls-[$Co^{II}(SQ)_2$(phen)] 238 K (cobalt $S = {}^1/_2$, two $S = {}^1/_2$ SQ^- antiferromagnetically aligned)	VBP	−0.258	0.585	0.715	−0.044
	Xα				
ls-[Co^{III}(SQ)(Cat)(phen)] 173 K (cobalt $S = 0$, one $S = {}^1/_2$ SQ^-)	VBP	−0.096	−0.335	−0.581	0.012
	Xα	−0.109	−0.329	−0.582	0.018
ls-[Co^{III}(SQ)(Cat)(en)] 300 K (cobalt $S = 0$, one $S = {}^1/_2$ SQ^-	VBP	−0.181	−0.261	−0.585	0.001
	Xα	−0.199	−0.252	−0.569	0.007

Table 5. Net Charge Distribution for Fragments of Various Valence-Tautomeric States Obtained from Calculations Which Utilized VBP and Xα Potentials

		net charge			
complex	potential	Co	Cat(SQ_1)	SQ_2	N⌒N
hs-[$Co^{II}(SQ)_2$(phen)] 300K (cobalt $S = {}^3/_2$, two $S = {}^1/_2$ SQ^- ferromagnetically aligned)	VBP	0.949	−0.590	−0.585	0.229
	Xα	0.808	−0.539	−0.534	0.264
hs-[$Co^{II}(SQ)_2$(phen)] 300 K (cobalt $S = {}^3/_2$, two $S = {}^1/_2$ SQ^- antiferromagnetically aligned)	VBP	0.911	−0.525	−0.502	0.117
	Xα	0.762	−0.457	−0.435	0.129
ls-[$Co^{II}(SQ)_2$(phen)] 238 K (cobalt $S = {}^1/_2$, two $S = {}^1/_2$ SQ^- ferromagnetically aligned)	VBP	0.864	−0.571	−0.555	0.260
	Xα				
ls-[$Co^{II}(SQ)_2$(phen)] 238K (cobalt $S = {}^1/_2$, two $S = {}^1/_2$ SQ^- antiferromagnetically aligned)	VBP	0.858	−0.618	−0.569	0.331
	Xα				
ls-[Co^{III}(SQ)(Cat)(phen)] 173 K (cobalt $S = 0$, one $S = {}^1/_2$ SQ^-)	VBP	0.843	−0.682	−0.563	0.405
	Xα	0.663	−0.616	−0.500	0.453
ls-[Co^{III}(SQ)(Cat)(en)] 300 K (cobalt $S = 0$, $S = {}^1/_2$ SQ^-)	VBP	0.831	−0.774	−0.597	0.539
	Xα	0.660	−0.713	−0.544	0.598

the net spin densities and charges of the cobalt and ligands for each of the spin-aligned and broken symmetry states from the VBP and Xα calculations. The net spin densities of the ligands were obtained by summing the individual densities of each atom of the ligand. Net spin is simply the difference between α and β spin densities at an atom. Negative net spin density indicates a net β spin at the site, and a spin density of 1.0 indicates a single unpaired electron. Likewise, the charges on the ligands were obtained by summing over the atoms of the ligand. The charges in Table 5 are relative to the neutral atom or ligand. The VBP calculations display charges which are slightly higher, and spin densities which are slightly lower, than the Xα results, but both types of calculations show the same overall trends. Only the VBP results will be discussed in the following section.

The calculated net spin density distributions clearly show that the idealized character of the ligand and metal can be assigned on the basis of net spin distributions. Furthermore, convergence of the calculations to the correct valence tautomeric state is confirmed by the net spin density distribution. For example, spin-aligned *hs*-[$Co^{II}(SQ)_2$(phen)] has the idealized occupation scheme Co^{II} $d^5\alpha$ $d^2\beta$ ($S = {}^3/_2$), SQ_1 $\pi^{*1}\alpha$ $\pi^{*0}\beta$ ($S = {}^1/_2$), SQ_2 $\pi^{*1}\alpha$ $\pi^{*0}\beta$ ($S = {}^1/_2$) and formally has three unpaired electrons on the cobalt and one unpaired electron on each of the two semiquinonate ligands. The VBP net spin densities of 2.719 on the cobalt and 1.102 and 1.108 on each of the SQ^- ligands are quite close to this. Similarly, spin-aligned *ls*-[$Co^{II}(SQ)_2$-(phen)] has the idealized occupation scheme Co^{II} $d^4\alpha$ $d^3\beta$ ($S = {}^1/_2$), SQ_1 $\pi^{*1}\alpha$ $\pi^{*0}\beta$ ($S = {}^1/_2$), SQ_2 $\alpha^{*1}\alpha$ $\pi^{*0}\beta$ ($S = {}^1/_2$). This

Table 6. Total Bonding Energies of the Various Valence-Tautomeric States for VBP and Xα Calculations

complex	bonding energy (eV) VBP	Xα
hs-[$Co^{II}(SQ)_2$(phen)] 300K (cobalt $S = {}^3/_2$, two $S = {}^1/_2$ SQ^- ferromagnetically aligned)	−297.826	−318.349
hs-[$Co^{II}(SQ)_2$(phen)] 300 K (cobalt $S = {}^3/_2$, two $S = {}^1/_2$ SQ^- antiferromagnetically aligned)	−298.268	−317.594
ls-[$Co^{II}(SQ)_2$(phen)] 238 K (cobalt $S = {}^1/_2$, two $S = {}^1/_2$ SQ^- ferromagnetically aligned)	−298.554	
ls-[$Co^{II}(SQ)_2$(phen)] 238 K (cobalt $S = {}^1/_2$, two $S = {}^1/_2$ SQ^- antiferromagnetically aligned)	−298.355	
ls-[Co^{III}(SQ)(Cat)(phen)] 173 K (cobalt $S = 0$, one $S = {}^1/_2$ SQ^-)	−298.964	−319.730

state formally has a single unpaired electron on the cobalt and a single unpaired electron on each of the SQ^- ligands. The VBP net spin densities of 1.276 on the cobalt and 0.850 and 0.853 on each of the SQ^- ligands are clearly consistent with this description. Likewise, *ls*-[Co^{III}(SQ)(Cat)(phen)] and *ls*-[Co^{III} (SQ)(Cat)(en)] have the occupation scheme Co^{III} $d^3\alpha$ $d^3\beta$ ($S = 0$); Cat $\pi^{*1}\alpha$ $\pi^{*1}\beta$ ($S = 0$), SQ $\pi^{*0}\alpha$ $\pi^{*1}\beta$ ($S = {}^1/_2$). This state formally has a single unpaired electron on the SQ^- ligand. The calculated net spin densities show that the unpaired spin density is delocalized predominately over the SQ^- ligand, but a substantial amount is also delocalized over the Cat^{2-} with a smaller, but significant, amount on the cobalt ion.

The BS states show clearly the flipping of spins at the cobalt which is necessary when going from the spin-aligned state to the antiferromagnetic broken symmetry state. Furthermore, these $M_s = {}^1/_2$ BS states provide insight into the spin-allowed valence-tautomeric interconversion process and show similarities with the *ls*-[Co^{III}(SQ)(Cat)] valence-tautomeric state. The BS *hs*-[$Co^{II}(SQ)_2$(phen)] state has the idealized occupation scheme Co^{II} $d^2\alpha$ $d^5\beta$ ($S = {}^3/_2$), SQ_1 $\pi^{*1}\alpha$ $\pi^{*0}\beta$ ($S = {}^1/_2$), SQ_2 $\pi^{*1}\alpha$ $\pi^{*0}\alpha$ ($S = {}^1/_2$). This state formally is expected to have three unpaired electrons antiferromagnetically coupled to the two SQ^- unpaired electrons. The net spin densities are close but show some deviation from the ideal situation. It can be seen in Table 4 that the spin has been flipped at the cobalt ion but its magnitude has decreased to −2.313. Similarly, the net spin densities at the SQ^- ligands are less than expected, which is due to some electron spin transfer between the cobalt and the SQ ligands. Also, some asymmetry in spin distribution is beginning to occur between the *o*-quinone ligands, and some unpaired spin density has been delocalized out onto the phen ligand. (Note that because there is no symmetry, the two SQ^- ligands are symmetry inequivalent in the 300 K structure, and even the internal geometries are slightly different; the observed spin asymmetry between the two SQ^- ligands is feasible given this geometric inequivalence.)

The BS *ls*-[$Co^{II}(SQ)_2$(phen)] state has the idealized occupation scheme Co^{II} $d^3\alpha$ $d^4\beta$ ($S = {}^1/_2$), SQ_1 $\pi^{*1}\alpha$ $\pi^{*0}\beta$ ($S = {}^1/_2$), SQ_2 $\pi^{*1}\alpha$ $\pi^{*0}\beta$ ($S = {}^1/_2$). This state formally has a single unpaired electron on the cobalt ion antiferromagnetically coupled to single unpaired electrons on each of the SQ^- ligands. However, the BS state for the *ls*-Co^{II} tautomer shows a net spin-density distribution which, while distinctive, shows some similarities to the *ls*-Co^{III} configuration. Some spin density from the cobalt ion has been transferred back as minority spin density to the SQ_1 ligand, making it more similar to Cat^{2-}, and thus the *ls*-Co^{II} state has similarities to the *ls*-Co^{III} state. The net spin density at the cobalt has decreased to −0.258, while the net spin density at SQ_1 is 0.585 and at SQ_2 is 0.715. A close look at the idealized ligand field diagrams in Figure 12A,B reveals the similarities between the electronic structures of these two states.

As shown in Table 5 the charge distribution of the various valence-tautomeric states deviates substantially from a formal ionic oxidation state picture and implicates an appreciable degree of covalency in the bonding. In a formal oxidation-state picture the SQ^- would carry a 1− charge, the Cat^{2-} ligand would carry a 2− charge, and depending on the valence-tautomeric state, the cobalt would carry a 2+ or 3+ charge. The *ls*-[Co^{III}(SQ)-(Cat)(en)] complex clearly shows distinct charges on the Cat^{2-} and SQ^- ligands which are less than expected from a formal ionic picture. The Cat^{2-} ligand has a charge of −0.774, and the SQ^- ligand has a charge of −0.597. Similarly, the corresponding (phen) complex has a Cat^{2-} charge of −0.68 and SQ^- of −0.56. This compares to the spin-aligned *hs*-[$Co^{II}(SQ)_2$-(phen)] case where SQ_1 and SQ_2 hold calculated charges of −0.590 and −0.585, respectively. The charge at the cobalt ion is substantially less than what is expected from the formal oxidation states and shows a slight decrease with increasing formal oxidation state. This decrease is opposite to the trend expected for formal oxidation states and likely reflects the shorter metal−ligand bond lengths in the Co^{III} complex which allows for a greater metal−ligand covalency and places more positive charge out onto the counter ligand.

EPR spectroscopy has been used to show that the unpaired spin density in *ls*-Co^{III} complexes with coordinated SQ^- ligands resides predominately on the SQ^- ligand.[11] However, some spin density is delocalized onto the cobalt ion since eight-line isotropic EPR signals centered around $g = 2.0$ are usually observed due to weak hyperfine coupling of 10−30 G to the ^{59}Co($I = {}^7/_2$) nucleus. In fact, experimentally it was found[11b] that [Co(3,6-DTBSQ)(3,6-DTBCat)(tmeda)] (the atomic coordinates for the en complex were derived from this complex) in toluene solution at 77 K shows an isotropic spectrum with two components, $g_1 = 2.0101$ and $g_2 = 2.0005$, each coupled to the cobalt nucleus with constants of $A_1 = 32$ G and $A_2 = 27$ G. These couplings of 32 and 27 G are the largest ones to date found for *ls*-Co^{III} semiquinonate complexes. The *ls*-[Co^{III}(SQ)-(Cat)(en)] complex (noting $M_s = -{}^1/_2$, so the total number of unpaired electrons equals −1) has calculated spin densities of −0.585, −0.261, and −0.181 on the SQ^-, Cat^{2-}, and cobalt ion, respectively. The *ls*-[Co^{III}(SQ)(Cat)(phen)] complex has calculated spin densities of −0.581, −0.335, and −0.096 on the SQ^-, Cat^{2-}, and cobalt ion, respectively. The unpaired spin density in these complexes is located mainly in molecular orbitals composed of $3b_1$ π^* orbitals of the ligands and t_{2g} orbitals of the cobalt ions. For both complexes the unpaired spin density distribution closely resembles the LUMO's 62α for the en complex and 82α for the phen complex (Figure 9). The en complex, which has a calculated spin density at the cobalt ion of −0.181, is expected to have a large degree of hyperfine coupling to the metal center. The smaller hyperfine coupling of 20 G observed for *ls*-[Co^{III}(3,5-DTBSQ)(3,5-DTBCat)(phen)] in toluene solution is in agreement with the smaller calculated net spin density of −0.096 at the cobalt center.

(L) Magnetic Exchange Interactions and Total Bonding Energies. One goal of the present work was to calculate the energy separations between the various tautomeric forms of complex **1**. The calculated bonding energies for complex **1** are listed in Table 6. The bonding energies listed are with respect to the spin-restricted atoms as computed by the energy difference method. It can be seen that in going from the Xα to the VBP potential the computed bonding energies vary substantially. This

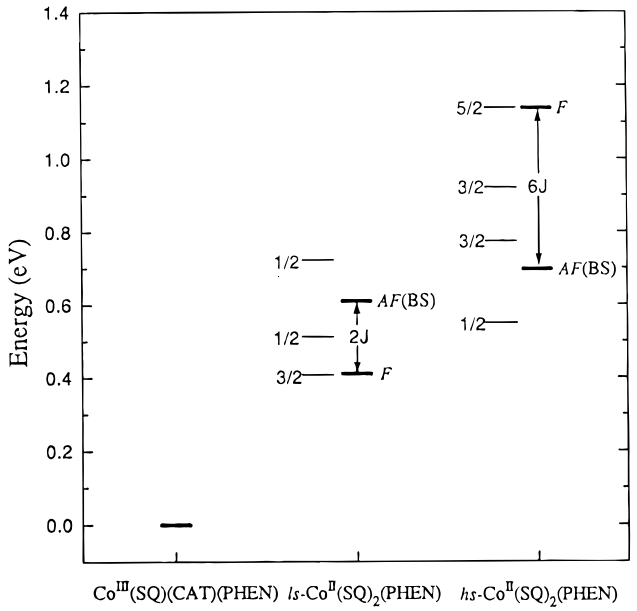

Figure 13. Plot of the energy separations between the various valence-tautomeric states of the Co^{II}−phen complex relative to the energy of the *ls*-[Co^{III}(SQ)(Cat)(phen)] state that is taken as 0. The energies are obtained from a difference between the total bonding energies. Located next to spin-aligned and broken symmetry energy levels are the energies of the pure spin states.

is a reflection of the different potentials used. The variational energy minimum principle does not apply when one density functional potential is being compared to the next. However, it does apply when energies within a single type of potential are compared. Furthermore, in order to obtain the true bonding energies the physical molecular bonding energy should be defined with respect to the spin-polarized atom fragments with the same potential and energy correction terms. This is not pursued here. Instead, we are concerned with the relative bond energies (a) for the calculation of the magnetic exchange interactions present in *hs*-[$Co^{II}(SQ)_2$(phen)] and *ls*-[$Co^{II}(SQ)_2$-(phen)] and (b) for the calculation of the energy separations between the valence-tautomeric states.

In the case of the *hs*-[$Co^{II}(SQ)_2$(phen)] complex, calculations were carried out for the spin-aligned hs-[$Co^{II}(SQ)_2$(phen)] state, where the spins of the *hs*-Co^{II} ion and the two SQ^- ligands are parallel, and for the broken symmetry *hs*-[$Co^{II}(SQ)_2$(phen)] state. With Clebsch−Gordon coupling coefficients it is possible to show that the difference in energy between these two states ($E_{HS} - E_{BS}$) is $-6J$, where J is the exchange parameter from the spin Hamiltonian $\hat{H} = \sum_{i>j} - 2J\hat{S}_i \cdot \hat{S}_j$ that gauges the magnetic exchange interactions between the *hs*-Co^{II} ion and the two coordinated SQ^- ligands. Likewise, for the hypothetical *ls*-[$Co^{II}(SQ)_2$(phen)] complex the energy separation between the high-spin and broken symmetry states can be shown to be $-2J$.

Figure 13 displays in graphical form the calculated energies (VBP potential) of the two different Co^{II} valence-tautomeric states relative to the calculated ground-state energy of the *ls*-[Co^{III}(SQ)(Cat)(phen)] complex. The pure spin state energies, shown together with the energies of the high-spin and for broken symmetry states, have been calculated from the J value obtained from the energy separation between the ferromagnetic high-spin and broken symmetry states. It is clear that these LCAO calculations give the *ls*-Co^{III} tautomer as the ground state, which is in agreement with experiment. Furthermore, the calculated average energies of the valence tautomeric states follow the trend

$$ls\text{-}[Co^{III}(SQ)(Cat)] < ls\text{-}[Co^{II}(SQ)_2] < hs\text{-}[Co^{II}(SQ)_2]$$

Experimentally, from solution magnetic susceptibility measurements we have determined that the *hs*-Co^{II} state lies at ∼2238 cm^{-1} (=ΔH) above the ground *ls*-Co^{III} state. This compares well to our calculated lowest energy $S = {}^1/_2$ *hs*-Co^{II} state which the density functional calculations indicate lies 4428 cm^{-1}(0.55 eV) above the *ls*-Co^{III} ground state. The magnetic exchange interaction between the *hs*-Co^{II} ion and the SQ^- ligand in *hs*-[$Co^{II}(SQ)_2$(phen)] was calculated to be antiferromagnetic in nature with $J = -594$ cm^{-1}(−0.07 eV). This compares to the experimental J value of -30 cm^{-1} evaluated for the *hs*-Co^{II}-$(SQ)_2$ units of the [Co_4(3,5-DTBSQ)$_8$] tetrameric complex.[42] For the *ls*-[$Co^{II}(SQ)_2$(phen)] complex the exchange parameter was calculated to be $J = +802$ cm^{-1} (0.10 eV) and is ferromagnetic in nature. The ferromagnetic interaction is expected in this case since the unpaired electron on the cobalt ion occupies an e_g* type orbital that interacts with the in-plane SQ^- σ-type orbitals and is therefore approximately orthogonal to the unpaired electrons in the SQ^- π*-type orbitals. These unpaired electrons are not expected to interact very effectively. Although the calculated energies are larger than what was observed experimentally, it must be kept in mind that we are calculating energy differences in the range of 0.2−0.4 eV for $E_{HS} - E_{BS}$ (and J parameters of 0.1 eV), while the total bonding energies of the complexes are ∼300 eV. Overall, the calculations display the expected energy level orderings, but the energy differences are larger than expected.

(M) Counter-Ligand Effects and Ligand Field Splittings. In previous work[9,39] we have shown that we can subtly vary the energy separations between Co^{III} and Co^{II} tautomers by utilizing different counter ligands. The temperature ($T_{1/2}$) at which there are equal amounts of the *ls*-Co^{III} and *hs*-Co^{II} tautomers present in solution has been varied from 350 K for the counter ligand as 4,4′-diphenyl-2,2′-bipyridine to $T_{1/2} < 180$ K for bipyrazine as L in *hs*-[$Co(SQ)_2$(L)]. The variation in $T_{1/2}$ in response to changes in the counter ligand and fundamentally the energy separations between the Co^{III} and Co^{II} valence tautomers can be explained by a synergistic effect of σ-donating and π-back-bonding ability of the counter ligand. It was observed that the $T_{1/2}$ correlated with the first reduction potential of the counter ligand.[9b] The first reduction potential gives an indication of the energy of the first π* LUMO of the counter ligand since it is in this orbital that the reducing electron is placed. As the reduction potential of the counter ligand increases (becomes more positive), the critical temperature decreases, which implies that the energy separation between Co^{III} and Co^{II} forms decreases.

The observed ligand field splittings are fundamentally tied to σ-donating and π-back-bonding abilities of all the ligands. Changes in σ-donating abilities of the ligands alter the energy of the e_g* antibonding levels, while π* back-bonding will tend to alter the energies of the t_{2g} set. The mean ligand field splitting tends to decrease from *ls*-Co^{III} to *ls*-Co^{II} to *hs*-Co^{II} valence-tautomeric states since the average metal−ligand bond lengths change from 1.904 to 2.028 to 2.081 Å, respectively. Figure 14 shows the position of the ligand field levels for the valence-tautomeric states of the phen and en complexes obtained from calculations utilizing a VBP potential. Since metal−ligand covalency and exchange coupling can spread metal character over multiple molecular orbitals and energy ranges, the average cobalt t_{2g} and e_g orbital energies have been calculated as Mulliken population weighted averages. The ligand field splitting of the *ls*-[Co^{III}(SQ)(Cat)(en)] in Figure 14A is 2.62 eV in the α and 2.657 eV in the β spin manifold. The ligand

(42) Lynch, M. W.; Buchanan, R. M.; Pierpont, C. G.; Hendrickson, D. N. *Inorg. Chem.* **1981**, *20*, 1038.

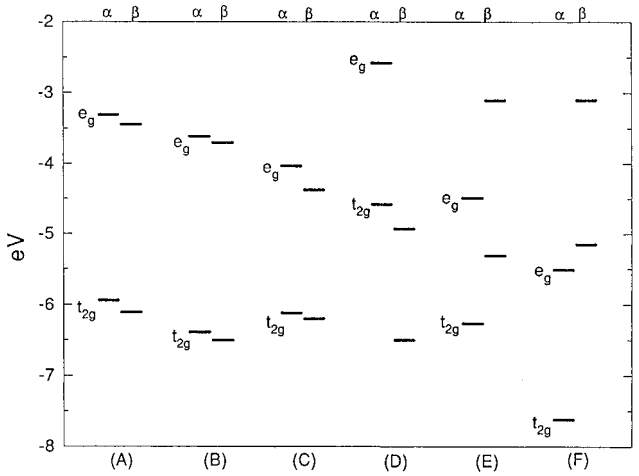

Figure 14. Plot of the ligand field splittings for the valence-tautomeric states showing the average energy level positioning of the t_{2g} and e_g* cobalt orbitals: (A) *ls*-[Co^{III}(SQ)(Cat)(en)]; (B) *ls*-[Co^{III}(SQ)(Cat)-(phen)]; (C) BS *ls*-[$Co^{II}(SQ)_2$(phen)]; (D) BS *hs*-[$Co^{II}(SQ)_2$(phen)]; (E) spin-aligned *ls*-[$Co^{II}(SQ)_2$(phen)]; and (f) spin-aligned *hs*-[$Co^{II}(SQ)_2$-(phen)].

field splitting of the *ls*-[Co^{III}(SQ)(Cat)(phen)] state shown in Figure 14B has a slightly larger splitting of 2.77 eV in α and 2.79 eV in β. The conversion from the *ls*-Co^{III} to the *ls*-Co^{II} tautomer results in an increase of the average metal−ligand bond length of 0.124 Å. (This assumes that the *ls*-Co^{II} complex has the geometry of the intermediate T = 238 K structure.) Consequently, the ligand field splitting for the BS *ls*-Co^{II} system, Figure 14C, has decreased to 2.07 eV in the α and 1.82 eV in the β spin manifold. The additional increase (with respect to *ls*-Co^{II}) in the metal−ligand bond lengths by 0.053 Å (300 K structure) results in a ligand field splitting for the BS *hs*-Co^{II} state, Figure 14D, of 1.82 eV in the α and 1.57 eV in the β spin manifold. The ligand field splitting of the spin-aligned *ls*-[$Co^{II}(SQ)_2$(phen)] state, Figure 14E, is 1.771 eV in the α and 2.208 eV in the β spin manifold. Finally, the splitting for "ferromagnetic" *hs*-[$Co^{II}(SQ)_2$(phen)], Figure 14F, is 2.112 eV in the α and 2.051 eV in the β spin manifold.

Greater σ donation tends to stabilize the *ls*-Co^{III} state relative to the *ls*-Co^{II} and *hs*-Co^{II} valence-tautomeric states. For the *ls*-Co^{III} tautomer greater σ donation increases the energy of the empty e_g* antibonding orbitals, placing them energetically well above the $3b_1$ π* levels of the SQ^- and Cat^{2-} ligands. Furthermore, the filled e_g bonding levels are lowered in energy, resulting in an overall more negative total bonding energy. Conversely, greater σ donation can destabilize the *ls*-Co^{II} tautomer relative to the *ls*-Co^{III} tautomer by shifting the energy of the e_g* levels above the $3b_1$ π* orbitals. In Figures 12B and 11B it can be seen that these orbitals lie very close in energy. Spin polarization splitting helps to stabilize the e_g* orbitals in the β spin manifold. However, large σ donation and destabilization of the e_g* orbital hinders transfer of the electron from the Cat^{2-} ligand to the cobalt ion (compare Figure 12A,B) and ultimately leads to an increase in the energy of the *ls*-Co^{II} state with respect to the *ls*-Co^{III} state. Greater σ donation will also tend to increase the energy of the *hs*-Co^{II} valence-tautomeric state. As the e_g* levels are moved higher in energy due to greater σ donation, the spin polarization energy may become smaller than the ligand field splitting and the *ls*-Co^{II} state will become favored compared to the *hs*-Co^{II} state. Figure 12C shows that the spin polarization splitting only slightly exceeds the ligand field splitting and that the e_g* orbitals are relatively close in energy to the π* orbitals of the SQ^- ligand and to the empty t_{2g} level.

π-Back-bonding is important in the *hs*-Co^{II} valence tautomer, since the minority spin t_{2g} orbital levels are substantially raised in energy, becoming close to the π* levels of the diiminium ligand as a result of spin polarization splitting. Depending on the symmetries and energies of these π* levels at the counter-ligand, back-bonding may increase or decrease the energies of the t_{2g} set and consequently the total bonding energy. The broken symmetry *hs*-Co^{II} state HOMO orbital 81α is a predominately cobalt t_{2g} orbital, but it contains a contribution from the π* phenanthroline ligand of 4.5%. Orbitals 83α and 84α are phen π* orbitals (86.8% and 93.7%, respectively) that have contributions from the metal t_{2g} set of 13.2% and 6.4%, respectively. This situation corresponds to a back-bonding interaction. The t_{2g} levels are stabilized in energy while the corresponding phen π* levels are destabilized. In this case a portion of the minority α spin density, 0.117 of an electron, is placed onto the phenanthroline ligand.

π-Back-bonding fundamentally serves to stabilize the *hs*-Co^{II} state relative to the *ls*-Co^{II} and *ls*-Co^{III} states by lowering the energy of the minority spin t_{2g} set. An example of this effect is nicely displayed by comparing the calculated ligand field splittings for the *ls*-Co^{III} phen and en complexes with the experimental $T_{1/2}$ values for the complexes in solution. The $T_{1/2}$ values for the phenanthroline and the tmeda complexes are 226.6 and 310 K, respectively. It would appear then that the phenanthroline complex has a smaller energy separation between Co^{III} and Co^{II} valence-tautomeric states. However, the calculated ligand field splittings for the *ls*-Co^{III} forms are ∼2.70 eV for the phen complex and ∼2.64 eV for the en complex. This indicates that the σ-donating capabilities of the ligands are roughly similar. This effect alone would imply that the $T_{1/2}$ temperatures should be similar for the two complexes. However it is likely that the π interactions which are only possible in the phen case are serving to stabilize the *hs*-Co^{II} states relative to the *ls*-Co^{III} state, ultimately leading to a lower $T_{1/2}$. Some evidence for π-back-bonding in the *hs*-Co^{II} tautomer is given in Table 4, where it can be seen that the net spin is 0.117 for the phen ligand in *hs*-[$Co^{II}(SQ)_2$(phen)]. The net spin on the phen ligand in the *ls*-Co^{III} tautomer is an order of magnitude smaller. Thus, the σ-donation and π-back-bonding characteristics of the counter ligand may affect the energy difference beween *ls*-Co^{III} and *hs*-Co^{II} tautomers.

(N) Optical Transitions. In order to interpret the complicated electronic absorption spectra of these complexes, theoretical calculations of the electronic excitation energies for the en and phen complexes were carried out. As a first approximation to excitation energies, the differences between one-electron energies of the appropriate virtual and occupied molecular orbitals may be used. Density functional calculations, in contrast to Hartree−Fock calculations, provide a reasonable estimate of the energies of virtual orbitals. For the en complex, additional SCF calculations of excited states have been performed, which correspond to Franck−Condon type transitions. The electrons of the excited state are allowed to relax in the nuclear configuration of the ground state. The difference in the total bonding energy of the ground and excited states, ΔSCF, provides the energy of the particular transition.

In the case of the *ls*-[Co^{III}(SQ)(Cat) N⌒N)] type of complex the exact origin of the ∼2500 nm low-energy electronic transition has been the subject of some speculation. The band has been given two possible assignments. On the one hand, the band has been assigned as a direct LMCT transition from the highest occupied Cat^{2-} $3b_1$ π* orbital to the lowest unoccupied cobalt e_g* molecular orbital.[11b] Such a transition is a LMCT transition from the Cat^{2-} ligand to the *ls*-Co^{III} ion,

giving a *ls*-$Co^{II}(SQ)_2$ excited state. An alternative assignment for the low-energy band is that it is the IT transition from the HOMO Cat^{2-} $3b_1$ π^* to the LUMO SQ^- $3b_1$ π^*, that is, simply an intervalence transfer from the Cat^{2-} to the SQ^- ligand. Both transitions are spin-allowed transitions, since exchange coupling in the *ls*-[$Co^{II}(SQ)_2$] complexes gives a spin ladder with a $S = {}^1/_2$ state (in fact, with two $S = {}^1/_2$ states at different energies, see Figure 13). However, the LMCT transition is orbitally forbidden, because it involves a transition between nearly orthogonal orbitals and therefore is expected to be weak in intensity. The observed molar extinctions of $\epsilon > 2000$ cm^{-1} M^{-1} are not consistent with an orbitally forbidden transition. Simpler model complexes have been made that have only a single 3,5-DTBCat^{2-} ligand bound to a *ls*-Co^{III} ion such as in the *ls*-[Co^{III}(CTH)(3,5-DTBCat)](PF_6), where CTH is an aliphatic tetradentate nitrogen macrocycle, and this complex shows its lowest energy transition at 12 000 cm^{-1}.[43] These low-energy transitions have molar extinctions of ~200 cm^{-1} M^{-1} and have been assigned as the Cat^{2-} $3b_1$ π^* to Co e_g* transition. Furthermore, the lowest energy transition shifts to higher energy when the tetrachloro catecholate ligand is used, which is to be expected since the $3b_1$ π^* orbitals are lowered in energy relative to the e_g* orbitals. Conversely, mixed-valence organic molecules which have two *p*-quinone moieties in differing oxidation states show intense low-energy transitions in the 1500−2200 nm (6666−4545 cm^{-1}) range with molar extinctions that range from ~2000 to ~30 000 cm^{-1} M^{-1}.[44] It seems probable that the lowest energy near-IR transition seen for these cobalt valence-tautomeric complexes is an intramolecular IT transition between Cat^{2-} and SQ^- ligands.

For the *ls*-[Co^{III}(SQ)(Cat)(en)] complex separate SCF calculations were performed for each of the electronic transitions marked in the molecular orbital energy level diagram of Figure 9A. Table 7 lists the total bonding energy of the ground and excited states. ΔE (SCF) energies are listed in units of both eV and cm^{-1}. One-electron orbital energy differences from the ground state are listed in parentheses. The lowest energy transition involves an intervalence transfer of an electron from the predominately Cat^{2-} $3b_1$ π^* HOMO (orbital 61α) to the SQ^- $3b_1$ π^* LUMO (orbital 62α). Although these orbitals are somewhat mixed, the transition is essentially a transfer of an electron from the Cat^{2-} to the SQ^- ligand. Table 8 lists the net spin densities of the ground and excited states of the en complex. The net spin density of the IT excited state shows that the Cat^{2-} contains the majority of the unpaired spin density (−0.674) since an electron from its filled $3b_1$ π^* orbital has been transferred to the SQ^- ligand. The experimentally observed lowest energy transition of the analogous tmeda complex **2** has its maximum absorption at an energy of 4086 cm^{-1} with ϵ ~4000 cm^{-1} M^{-1}. The theoretically calculated energy of the lowest energy IT transition for the en complex is 5323 cm^{-1}. Thus, we have to conclude that the experimentally observed lowest energy transition is assigned to an IT transition, which is compatible with the observed absorption intensity.

The transition from HOMO 62β to LUMO 63β is the lowest energy LMCT and is labeled as LMCT1. This spin-allowed transition involves the transfer of an electron from the filled Cat^{2-} $3b_1$ π^* orbital to the e_g* orbital of the cobalt. The spin density of the excited state displays the *ls*-[$Co^{II}(SQ)_2$] configuration, where the net spin density at the cobalt is −0.929 and

Table 7. ΔSCF Transition Energies and One-Electron Molecular Orbital Energy Differences (Shown in Parentheses)of Some Electronic Transitions

	energy (eV)	ΔE (eV)	ΔE (cm^{-1})	exptl (cm^{-1})
		ls-[Co^{III}(SQ)(Cat)(en)]		
ground state	−216.83			
IT 61α → 62α	−216.17	0.66 (0.38)	5323 (3065)	4086
LMCT1 62β → 63β	−215.62	1.21 (0.93)	9759 (7460)	10000 sh
LMCT2 60α → 63α	−215.25	1.58 (1.93)	12743 (15565)	
$\pi-\pi^*$ 56α → 62α	−214.54	2.29 (2.23)	18067 (17984)	15384
$\pi-\pi^*$ 60α → 62α		(1.15)	(9275)	~9000
		ls-[Co^{III}(SQ)(Cat)(phen)]		
IT 81α → 82α		(0.153)	(1232)	4000
$LMCT_1$ 82β → 85β		(0.946)	(7629)	10000 sh
$LMCT_2$ 80α → 85α		(2.01)	(16180)	
$\pi-\pi^*$ 76α → 82α		(2.325)	(18730)	16666
$\pi-\pi^*$ 80α → 82α		(1.235)	(9960)	~9000
		hs-[$Co^{II}(SQ)_2$(phen)]		
MLCT 79β → 84β		(1.310)	(10565)	12820
LF 79β → 85β		(2.265)	(18246)	18348

Table 8. Net Spin Densities of the States Resulting from the ΔSCF Electronic Transitions for *ls*-[Co^{III}(SQ)(Cat)(en)]

		net spin			
	potential	Co	Cat	SQ	EDA
ground state	VBP	−0.181	−0.261	−0.585	0.001
IT 61α → 62α	VBP	−0.244	−0.674	−0.070	−0.013
LMCT1 62β → 63β	VBP	−0.929	0.423	−0.405	−0.091
LMCT2 60α → 63α	VBP	−0.289	−0.330	−0.537	0.158

where the antiparallel arrangement of net spin density at the ligands is +0.423 and −0.405. (Aside from the different counter ligand and geometry, this corresponds to the lower *ls*-[$Co^{II}(SQ)_2$] state with $S = {}^1/_2$ (Figure 13); the higher $S = {}^1/_2$ state corresponds to 61α → 63α and should be about 1600 cm^{-1} higher in energy, and of similar intensity.) The transition LMCT1 is orbitally forbidden and is expected to be weak in intensity. The calculated energy of this second lowest energy transition is 9759 cm^{-1}. The shoulder that appears at ~10 000 cm^{-1} for complex **2** and in other *ls*-[Co^{III}(SQ)(Cat)] complexes is likely due in part to this second lowest energy transition

The transition LMCT2 involves the transfer of an electron from π orbital 60α to cobalt e_g* orbital 63α. This transition is essentially ligand field in nature, but does contain some charge transfer from the Cat^{2-} π orbital to the cobalt. Overall the transition results in little net spin density change in the complex. This transition is the lowest energy transition originating in π type orbitals 56α through 60α and involving an excitation of an electron to the e_g* orbitals. The transition LMCT2 has a calculated energy of 12 743 cm^{-1}. LMCT2 type transitions are expected to be weak and are likely buried under the more intense transitions occurring in the visible region of the spectrum.

The transition marked $\pi-\pi^*$ for the *ls*-[Co^{III}(SQ)(Cat)(en)] complex (in Figure 9A) is the highest energy transition

(43) Benelli, C.; Dei, A.; Gatteschi, D.; Pardi, L. *Inorg. Chim. Acta*, **1989**, *163*, 99.
(44) (a) Jozefiak, T. H.; Miller, L. L. *J. Am. Chem. Soc.* **1987**, *109*, 6560. (b) Liberko, C. A.; Miller, L. L.; Katz, T. J.; Longbin, L. *J. Am. Chem. Soc.* **1993**, *115*, 2478. (c) Yang, B. W.; Liu, L.; Katz, T. J.; Liberko, C. A.; Miller, L. L. *J. Am. Chem. Soc.* **1991**, *113*, 8993.

representative of a progression of transitions which originate in 56α−60α orbitals and involve excitation to the LUMO 3b1 π^* orbital 62α. These transitions are spin and orbitally allowed and are expected to dominate the visible spectrum of these complexes. Experimentally, complex **2**, like similar *ls*-Co^{III} complexes, has its highest intensity visible absorption band centered at 15 384 cm^{-1} with an intensity of $\epsilon \sim 3000$ cm^{-1} M^{-1}. Strong absorption extends out to 9000 cm^{-1}. The highest energy $\pi-\pi^*$ transition from the 56α to the 62α orbital has a calculated transition energy of 18 067 cm^{-1}. The lowest energy $\pi-\pi^*$ transition from the 60α to the 62α orbital has a one-electron orbital energy difference of 9275 cm^{-1}. The majority of the intense visible transitions are likely due to these $\pi-\pi^*$ type transitions.

SCF calculations of the excited states of the *ls*-[Co^{III}(SQ)(Cat)(phen)] complex were also attempted; however, the presence of the unoccupied π^* orbitals of the phenanthroline ligand led to convergence problems. Table 7 instead lists only the one-electron orbital energy differences. These one-electron orbital energy differences yield low excitation energies compared to the experimental values for IT and LMCT1. The analysis of the optical transitions of the phen complex is fundamentally similar to the analysis given above for the en complex. The experimental visible and near-IR spectra of complexes **1** and **2** are similar, with no major absorptions occurring in the spectrum of complex **2** due to the presence of the unoccupied π^* orbitals of the phenanthroline.

The molecular orbital energy level diagram in Figure 9B clearly shows that the IT transition is the lowest energy transition for the phen complex. The HOMO $3b_1$ π^* 81α and LUMO $3b_1$ π^* 82α calculated one-electron orbital energy difference is 1232 cm^{-1}. This compares to the experimentally observed energy of 4000 cm^{-1} for the maximum of the absorption band shown in Figure 6. The one-electron orbital energy difference is expected to be less than the energy obtained from a full ΔSCF calculation. For comparison, the en complex has a calculated orbital one-electron separation for the IT transition of 3065 cm^{-1} and the ΔSCF energy is 5323 cm^{-1}. It is expected that a full SCF calculation of the IT excited state of the phen complex would also yield a larger value. The HOMO-LUMO energy separation of the en complex is slightly larger since the LUMO 62α of the en complex is slightly raised in energy due to a larger antibonding interaction with the cobalt t_{2g} orbitals. The predicted and observed orbital energy separations for the LMCT1 and $\pi-\pi^*$ transitions are very similar to those obtained for the en complex. The 15 K spectrum of Figure 6 clearly shows the progression of bands (17000−9000 cm^{-1}) of the *ls*-Co^{III} tautomer which are likely associated with the $\pi-\pi^*$ type transitions. Also noteworthy is the shoulder which appears in the spectrum at 10 000 cm^{-1}, which could be associated with the LMCT1 transition.

The most prominent features in the visible spectrum of *hs*-[$Co^{II}(SQ)_2$] complexes (see the room temperature spectrum in Figure 6) are the intense MLCT transition at ∼12 000 cm^{-1} (780 nm) and a LF transition at 18 348 cm^{-1} (545 nm). These transitions are typical for Co^{II} valence tautomers. Shoulders that often appear on the high-energy side of the MLCT and LF transitions may be associated with the *ls*-Co^{II} tautomer. The Co^{II} spectra show no presence of a low-energy electronic transition in the near-infrared region. The molecular orbital energy level diagram, Figure 11A, shows the MLCT and LF transitions of the *hs*-Co^{II} tautomer with ferromagnetic alignment of spins.

The MLCT transitions are from the minority β spin t_{2g} orbitals 78β−79β to the SQ^- π^* and phen π^* orbitals 81β−84β. These transitions are orbitally and spin allowed. The one-electron orbital energy difference between orbitals 79β and 84β is 10 565 cm^{-1}. This calculated energy for the highest energy MLCT transition compares favorably with that found experimentally. The experimentally observed absorption maximum at 12 820 cm^{-1} ($\epsilon \sim 3300$ cm^{-1} M^{-1}) extends out to 10 000 cm^{-1} and has a resolved shoulder at 15 151 cm^{-1}.

The LF transitions originate in t_{2g} orbitals 78β−79β with a one-electron excitation to the unoccupied e_g* orbitals 85β and 86β. The calculated energy for the LF transition between orbitals 79β and 85β is 18348 cm^{-1}. The experimentally observed transition for complex **1** in toluene solution is 18 246 cm^{-1} with an intensity of $\epsilon \sim 2500$ cm^{-1} M^{-1}. This transition has likely stolen intensity from the high- and low-energy bands surrounding it. For comparison the *hs*-$[Co^{II}(H_2O)_6]^{2+}$ complex shows a transition at ∼18 181 cm^{-1} (550 nm) with $\epsilon \sim 10$ cm^{-1} M^{-1}.[45] It is likely that the ∼18 000 cm^{-1} transition seen in [$Co^{II}(SQ)_2$] complexes is a ligand field transition.

Concluding Comments

SCF nonlocal density functional molecular orbital calculations were carried out for the different valence tautomers of the phen−Co complex: *ls*-[Co^{III}(SQ)(Cat)(phen)], *hs*-[$Co^{II}(SQ)_2$(phen)], and the hypothetical complex *ls*-[$Co^{II}(SQ)_2$(phen)]. By employing broken symmetry states it was calculated that the parameter (J in $\hat{H} = -2J\hat{S}_i\cdot\hat{S}_j$) gauging a single $Co^{II}-SQ^-$ magnetic exchange interaction is $J = -594$ cm^{-1} (antiferromagnetic) for the *hs*-Co^{II} tautomer and $J = +802$ cm^{-1} (ferromagnetic) for the *ls*-Co^{II} tautomer. These coupling strengths are probably too large, but physical arguments support AF coupling for the *hs*-Co^{II} tautomer and F coupling for the *ls*-Co^{II} tautomer. In this way it was possible to calculate the energy difference between the *ls*-Co^{III} tautomer and the $S = {}^1/_2$ spin state of the *hs*-Co^{II} tautomer. This energy difference was calculated to be 4428 cm^{-1}, which compares favorably to the $\Delta H = 2238$ cm^{-1} value evaluated by fitting magnetic susceptibility data assuming a valence-tautomeric equilibrium in solution. Also, for comparison with experiment, the spin degeneracy weighted average of all of the *hs*-Co^{II} tautomer spin states lies 7400 cm^{-1} above the *ls*-Co^{III} ground state. The experimental ΔH value was obtained by assuming that the magnetic exchange interactions in the *hs*-Co^{II} tautomer are very small and ignoring any temperature dependencies in magnetic susceptibility due to spin−orbit interactions at the Co^{II} ion. Thus, the theoretically calculated ΔH value is in quite good agreement with the experimental ΔH value, given the assumptions made for the latter. In fact, it is interesting that such a small energy difference (∼0.5 eV) can be calculated so well given the fact the total binding energy of each complex is on the order of ∼300 eV. Thus, the ΔE value is ∼0.2% of the total binding energy of a complex.

Calculations were also completed for the *ls*-[Co^{III}(SQ)(Cat)(en)] complex. It was of interest to understand the influence of the counter ligand, phen *vs* en, on the valence-tautomeric equilibrium. With the phen complex the midpoint ($T_{1/2}$) occurs at 227 K, whereas when the phen ligand is replaced with tmeda (related to en), then $T_{1/2}$ is 310 K. The σ-donation and π-backbonding characteristics of the counter ligand were examined and found to be important.

The calculations have indicated several interesting features of the electronic structure in these complexes. All calculations were spin unrestricted, where the spin-up (α) and spin-down (β) electrons are calculated separately. This showed how important spin polarization effects are in determining whether

(45) Cotton, F. A.; Wilkinson, G. *Advanced Inorganic Chemistry*; John Wiley and Sons: New York, 1972.

a given complex is *ls*-[Co^{III}(SQ)(Cat)] or *hs*-[$Co^{II}(SQ)_2$], that is, when the cobalt is high spin or low spin and when it is favorable for intramolecular electron transfer between cobalt ion and a *o*-quinone-derived ligand. Large spin polarization splittings have also been seen in other systems with high-spin transition metal sites, particularly in ferric chlorides and ferric sulfide complexes.[41,46] These calculations also indicated the importance of covalent interactions in the Co valence-tautomeric complexes. Even though there are localized electronic charges and spin densities in a complex as suggested by formal oxidation-state descriptions such as *ls*-[Co^{III}(SQ)(Cat)], covalent interactions lead to appreciable mixing. A given molecular orbital may be largely Cat^{2-} π^* in nature, but it will also have contributions from the SQ^- ligand.

The calculations of optical transition energies are very promising, specifying the low energy of the catechol $\rightarrow$ semiquinone intervalence transfer band in the *ls*-Co^{III} system, and the higher energy bands from LMCT and $\pi \rightarrow \pi^*$ transitions. For the *hs*-Co^{II} tautomer, the positions of the MLCT and ligand field bands were found. All of these calculated transitions are in good agreement with the experimental spectral bands, and the calculated assignments are supported by experimental evidence of intensities and spectra in related systems.

These nonlocal density functional calculations suggest that a *ls*-[$Co^{II}(SQ)_2$(phen)] form of the complex could be as stable as the *hs*-[$Co^{II}(SQ)_2$(phen)] tautomer. There is no experimental evidence for the existence of this *ls*-Co^{II} form of the complex. Laser-flash studies on the nanosecond and picosecond time scales only give evidence for the *ls*-Co^{III} and *hs*-Co^{II} tautomers. Upon laser excitation of the *ls*-Co^{III} complex from its $S = {}^1/_2$ ground state to a $S = {}^1/_2$ LMCT excited state, there is very rapid intersystem crossing to the ground state of the *hs*-Co^{II} tautomer. Only the *hs*-Co^{II} to *ls*-Co^{III} relaxation is detected in the laser experiments. Furthermore, in variable-temperature studies of the electronic absorption spectra of various Co valence-tautomeric complexes, isosbestic points are seen, indicating the presence of only two species, the *ls*-Co^{III} and *hs*-Co^{II} complexes.

Acknowledgment. We are grateful for funding of this work by NSF Grant CHE-9420322 (D.N.H.) and NIH Grants GM43278 and GM50154 (L.N.). We thank Prof. E. J. Baerends and his group for use of the ADF codes. We also thank Prof. Andreas Hauser for help in collecting the variable-temperature electronic absorption spectra for complex **1** doped into polystyrene.

Supporting Information Available: Tables giving input parameters such as atomic coordinates and atomic orbital basis sets and results of calculations such as Mulliken population analyses and energies and primary contributions to all of the molecular orbitals (59 pages). Ordering information is given on any current masthead page.

IC9611812

(46) (a) Butcher, K. D.; Gebhard, M. S.; Solomon, E. I. *Inorg. Chem.* **1990**, *29*, 2067. (b) Butcher, K. D.; Didziulis, S. V.; Briat, B.; Solomon, E. I. *J. Am. Chem. Soc.* **1990**, *112*, 2231.